The Astrophysical Journal, 1000:231 (21pp), 2026 April 1 https://doi.org/10.3847/1538-4357/ae34af

Ring Asymmetry and Spin in M87*

Vadim Bernshteyn[1,2], Nicholas S. Conroy[3,171], Michi Bauböck[1], Paul Tiede[4,5], Abhishek V. Joshi[1,6], Ben S. Prather[1,7], Charles F. Gammie[3,1,6,8], The Event Horizon Telescope Collaboration, Kazunori Akiyama[9,10,5], Ezequiel Albentosa-Ruíz[11], Antxon Alberdi[12], Walter Alef[13], Juan Carlos Algaba[14], Richard Anantua[15,16,5,4], Keiichi Asada[17], Rebecca Azulay[11,18,13], Anne-Kathrin Baczko[19,13], David Ball[2], Bidisha Bandyopadhyay[20], John Barrett[9], Bradford A. Benson[21,22], Dan Bintley[23,24], Lindy Blackburn[4,5], Raymond Blundell[4], Katherine L. Bouman[25], Geoffrey C. Bower[23,24,26,27], Michael Bremer[28], Roger Brissenden[4], Silke Britzen[13], Avery E. Broderick[29,30,31], Dominique Broguiere[28], Thomas Bronzwaer[32], Sandra Bustamante[33], Douglas F. Carlos[34], John E. Carlstrom[35,22,36,37], Andrew Chael[38], Chi-kwan Chan[2,39,40], Dominic O. Chang[4,5], Koushik Chatterjee[41,5,4], Ming-Tang Chen[26], Yongjun Chen (陈永军)[42,43], Xiaopeng Cheng[44], Paul Chichura[36,35], Ilje Cho[44,45,12], John E. Conway[19], Thomas M. Crawford[22,35], Geoffrey B. Crew[9], Alejandro Cruz-Osorio[46,47], Yuzhu Cui (崔玉竹)[48], Brandon Curd[15,5,4], Rohan Dahale[12], Jordy Davelaar[49,50], Mariafelicia De Laurentis[51,52], Roger Deane[53,54,55], Jason Dexter[56], Vedant Dhruv[1], Indu K. Dihingia[57], Sheperd S. Doeleman[4,5], Sergio A. Dzib[13], Razieh Emami[4], Heino Falcke[32], Joseph Farah[58,59], Vincent L. Fish[9], Edward Fomalont[60], H. Alyson Ford[2], Marianna Foschi[12], Raquel Fraga-Encinas[32], William T. Freeman[61,62], Per Friberg[23,24], Christian M. Fromm[63,47,13], Antonio Fuentes[12], Peter Galison[5,64,65], Roberto García[28], Olivier Gentaz[28], Boris Georgiev[2], Ciriaco Goddi[34,66,67,68], Roman Gold[69,70,71], Arturo I. Gómez-Ruiz[72,73], José L. Gómez[12], Minfeng Gu (顾敏峰)[42,74], Mark Gurwell[4], Kazuhiro Hada[75,76], Daryl Haggard[77,78], Ronald Hesper[79], Dirk Heumann[2], Luis C. Ho (何子山)[80,81], Paul Ho[17,24,23], Mareki Honma[76,82,83], Chih-Wei L. Huang[17], Lei Huang (黄磊)[42,74], David H. Hughes[72], Shiro Ikeda[10,84,85,86], C. M. Violette Impellizzeri[87,60], Makoto Inoue[17], Sara Issaoun[4,50], David J. James[88,89], Buell T. Jannuzi[2], Michael Janssen[32,13], Britton Jeter[90,91], Wu Jiang (江悟)[42], Alejandra Jiménez-Rosales[32], Michael D. Johnson[4,5], Svetlana Jorstad[92], Adam C. Jones[22], Taehyun Jung[44,93], Tomohisa Kawashima[94], Garrett K. Keating[4], Mark Kettenis[95], Dong-Jin Kim[96], Jae-Young Kim[97], Jongsoo Kim[44], Junhan Kim[98], Motoki Kino[10,99], Jun Yi Koay[100,17], Prashant Kocherlakota[5,4], Yutaro Kofuji[76,83], Patrick M. Koch[17], Shoko Koyama[100,17], Carsten Kramer[28], Joana A. Kramer[13], Michael Kramer[13], Thomas P. Krichbaum[13], Cheng-Yu Kuo[101,17], Noemi La Bella[32], Deokhyeong Lee[102], Sang-Sung Lee[44], Aviad Levis[25], Shaoliang Li[23,24], Zhiyuan Li (李志远)[103,104], Rocco Lico[105,12], Greg Lindahl[106], Michael Lindqvist[19], Mikhail Lisakov[107], Jun Liu (刘俊)[13], Kuo Liu[42,43], Elisabetta Liuzzo[108], Wen-Ping Lo[17,109], Andrei P. Lobanov[13], Laurent Loinard[110,5,111], Colin J. Lonsdale[9], Amy E. Lowitz[2], Ru-Sen Lu (路如森)[42,43,13], Nicholas R. MacDonald[13], Jirong Mao (毛基荣)[112,113,114], Nicola Marchili[108,13], Sera Markoff[115,116], Daniel P. Marrone[2], Alan P. Marscher[92], Iván Martí-Vidal[11,18], Satoki Matsushita[17], Lynn D. Matthews[9], Lia Medeiros[117], Karl M. Menten[13,170], Hugo Messias[118,119], Izumi Mizuno[23,24], Yosuke Mizuno[57,120,47], Joshua Montgomery[78,22], Kotaro Moriyama[47,76], Monika Moscibrodzka[32], Wanga Mulaudzi[115], Cornelia Müller[13,32], Hendrik Müller[13], Alejandro Mus[66,105,121,122], Gibwa Musoke[115,32], Ioannis Myserlis[123], Hiroshi Nagai[10,82], Neil M. Nagar[20], Dhanya G. Nair[20,13], Masanori Nakamura[124,17], Gopal Narayanan[33], Iniyan Natarajan[4,5], Antonios Nathanail[125,47], Santiago Navarro Fuentes[123], Joey Neilsen[126], Chunchong Ni[30,31,29], Michael A. Nowak[127], Hiroki Okino[76,83], Héctor Raúl Olivares Sánchez[128], Feryal Özel[129], Daniel C. M. Palumbo[5,4], Georgios Filippos Paraschos[13], Jongho Park[130,17], Harriet Parsons[23,24], Nimesh Patel[4], Ue-Li Pen[17,29,131,132,133], Dominic W. Pesce[4,5], Vincent Piétu[28], Alexander Plavin[5,4,13], Aleksandar PopStefanija[33], Oliver Porth[115,47], Giacomo Principe[134,135,105], Dimitrios Psaltis[129], Hung-Yi Pu[136,137,17], Alexandra Rahlin[22], Venkatessh Ramakrishnan[138,90,91], Ramprasad Rao[4], Mark G. Rawlings[139,23,24], Luciano Rezzolla[47,140,141], Angelo Ricarte[5,4], Luca Ricci[142], Bart Ripperda[131,143,132,29], Jan Röder[12], Freek Roelofs[32], Cristina Romero-Cañizales[17], Eduardo Ros[13], Arash Roshanineshat[2], Helge Rottmann[13], Alan L. Roy[13], Ignacio Ruiz[123], Chet Ruszczyk[9], Kazi L. J. Rygl[108], León D. S. Salas[115], Salvador Sánchez[123], David Sánchez-Argüelles[72,73], Miguel Sánchez-Portal[123], Mahito Sasada[144,76,145], Kaushik Satapathy[2], Saurabh[13], Tuomas Savolainen[146,91,13], Karl-Friedrich Schuster[147], Zhiqiang Shen (沈志强)[42,43], Sasikumar Silpa[20], Randall Smith[4], Bong Won Sohn[44,93,45], Jason SooHoo[9], Kamal Souccar[33], Joshua S. Stanway[148], He Sun (孙赫)[149,150], Alexandra J. Tetarenko[151], Remo P. J. Tilanus[2,32,87,152], Michael Titus[9], Kenji Toma[153,154], Pablo Torne[123,13], Teresa Toscano[12], Efthalia Traianou[12,13], Sascha Trippe[155,156], Matthew Turk[157], Ilse van Bemmel[158], Huib Jan van Langevelde[95,87,159], Daniel R. van Rossum[32], Sebastiano D. von Fellenberg[131,13], Jesse Vos[160], Jan Wagner[13], Derek Ward-Thompson[148], John Wardle[161], Jasmin E. Washington[2], Jonathan Weintroub[4,5], Maciek Wielgus[12], Kaj Wiik[162,90,91], Michael F. Wondrak[32,163], George N. Wong[164,38], Jompoj Wongphexhauxsorn[142,13], Qingwen Wu (吴庆文)[165], Paul Yamaguchi[4], Aristomenis Yfantis[32], Doosoo Yoon[115], André Young[32], Ziri Younsi[166,47], Wei Yu (于威)[4], Feng Yuan (袁峰)[167], Ye-Fei Yuan (袁业飞)[168], Ai-Ling Zeng (曾艾玲)[12], J. Anton Zensus[13], Shuo Zhang[169], and Guang-Yao Zhao[13,12]

[1] Department of Physics, University of Illinois, 1110 West Green Street, Urbana, IL 61801, USA
[2] Steward Observatory and Department of Astronomy, University of Arizona, 933 N. Cherry Avenue, Tucson, AZ 85721, USA
[3] Department of Astronomy, University of Illinois, 1002 West Green Street, Urbana, IL 61801, USA; nconroy2@illinois.edu
[4] Center for Astrophysics |Harvard & Smithsonian, 60 Garden Street, Cambridge, MA 02138, USA
[5] Black Hole Initiative at Harvard University, 20 Garden Street, Cambridge, MA 02138, USA
[6] Illinois Center for Advanced Study of the Universe, 1110 West Green Street, Urbana, IL 61801, USA
[7] Los Alamos National Lab, Los Alamos, NM, 87545, USA
[8] National Center for Supercomputing Applications, 605 East Springfield Avenue, Champaign, IL 61820, USA
[9] Massachusetts Institute of Technology Haystack Observatory, 99 Millstone Road, Westford, MA 01886, USA
[10] National Astronomical Observatory of Japan, 2-21-1 Osawa, Mitaka, Tokyo 181-8588, Japan
[11] Departament d'Astronomia i Astrofísica, Universitat de València, C. Dr. Moliner 50, E-46100 Burjassot, València, Spain
[12] Instituto de Astrofísica de Andalucía-CSIC, Glorieta de la Astronomía s/n, E-18008 Granada, Spain
[13] Max-Planck-Institut für Radioastronomie, Auf dem Hügel 69, D-53121 Bonn, Germany
[14] Department of Physics, Faculty of Science, Universiti Malaya, 50603, Kuala Lumpur, Malaysia
[15] Department of Physics & Astronomy, The University of Texas at San Antonio, One UTSA Circle, San Antonio, TX 78249, USA
[16] Physics & Astronomy Department, Rice University, Houston, TX 77005-1827, USA
[17] Institute of Astronomy and Astrophysics, Academia Sinica, 11F of Astronomy-Mathematics Building, AS/NTU No. 1, Sec. 4, Roosevelt Road, Taipei 106216, Taiwan, R.O.C.
[18] Observatori Astronòmic, Universitat de València, C. Catedrático José Beltrán 2, E-46980 Paterna, València, Spain
[19] Department of Space, Earth and Environment, Chalmers University of Technology, Onsala Space Observatory, SE-43992 Onsala, Sweden
[20] Astronomy Department, Universidad de Concepción, Casilla 160-C, Concepción, Chile
[21] Fermi National Accelerator Laboratory, MS209, P.O. Box 500, Batavia, IL 60510, USA
[22] Department of Astronomy and Astrophysics, University of Chicago, 5640 South Ellis Avenue, Chicago, IL 60637, USA
[23] East Asian Observatory, 660 N. A'ohoku Place, Hilo, HI 96720, USA
[24] James Clerk Maxwell Telescope (JCMT), 660 N. A'ohoku Place, Hilo, HI 96720, USA
[25] California Institute of Technology, 1200 East California Boulevard, Pasadena, CA 91125, USA
[26] Institute of Astronomy and Astrophysics, Academia Sinica, 645 N. A'ohoku Place, Hilo, HI 96720, USA
[27] Department of Physics and Astronomy, University of Hawaii at Manoa, 2505 Correa Road, Honolulu, HI 96822, USA
[28] Institut de Radioastronomie Millimétrique (IRAM), 300 rue de la Piscine, F-38400 Saint-Martin-d'Hères, France
[29] Perimeter Institute for Theoretical Physics, 31 Caroline Street North, Waterloo, ON N2L 2Y5, Canada
[30] Department of Physics and Astronomy, University of Waterloo, 200 University Avenue West, Waterloo, ON N2L 3G1, Canada
[31] Waterloo Centre for Astrophysics, University of Waterloo, Waterloo, ON N2L 3G1, Canada
[32] Department of Astrophysics, Institute for Mathematics, Astrophysics and Particle Physics (IMAPP), Radboud University, P.O. Box 9010, 6500 GL Nijmegen, The Netherlands
[33] Department of Astronomy, University of Massachusetts, Amherst, MA 01003, USA
[34] Instituto de Astronomia, Geofísica e Ciências Atmosféricas, Universidade de São Paulo, R. do Matão, 1226, São Paulo, SP 05508-090, Brazil
[35] Kavli Institute for Cosmological Physics, University of Chicago, 5640 South Ellis Avenue, Chicago, IL 60637, USA
[36] Department of Physics, University of Chicago, 5720 South Ellis Avenue, Chicago, IL 60637, USA
[37] Enrico Fermi Institute, University of Chicago, 5640 South Ellis Avenue, Chicago, IL 60637, USA
[38] Princeton Gravity Initiative, Jadwin Hall, Princeton University, Princeton, NJ 08544, USA
[39] Data Science Institute, University of Arizona, 1230 N. Cherry Avenue, Tucson, AZ 85721, USA
[40] Program in Applied Mathematics, University of Arizona, 617 N. Santa Rita, Tucson, AZ 85721, USA
[41] Department of Physics, University of Maryland, 7901 Regents Drive, College Park, MD 20742, USA
[42] Shanghai Astronomical Observatory, Chinese Academy of Sciences, 80 Nandan Road, Shanghai 200030, People's Republic of China
[43] Key Laboratory of Radio Astronomy and Technology, Chinese Academy of Sciences, A20 Datun Road, Chaoyang District, Beijing, 100101, People's Republic of China
[44] Korea Astronomy and Space Science Institute, Daedeok-daero 776, Yuseong-gu, Daejeon 34055, Republic of Korea
[45] Department of Astronomy, Yonsei University, Yonsei-ro 50, Seodaemun-gu, 03722 Seoul, Republic of Korea
[46] Instituto de Astronomía, Universidad Nacional Autónoma de México (UNAM), Apdo Postal 70-264, Ciudad de México, Mexico
[47] Institut für Theoretische Physik, Goethe-Universität Frankfurt, Max-von-Laue-Straße 1, D-60438 Frankfurt am Main, Germany
[48] Institute of Astrophysics, Central China Normal University, Wuhan 430079, People's Republic of China
[49] Department of Astrophysical Sciences, Peyton Hall, Princeton University, Princeton, NJ 08544, USA
[50] NASA Hubble Fellowship Program, Einstein Fellow
[51] Dipartimento di Fisica "E. Pancini", Università di Napoli "Federico II", Compl. Univ. di Monte S. Angelo, Edificio G, Via Cinthia, I-80126, Napoli, Italy
[52] INFN Sez. di Napoli, Compl. Univ. di Monte S. Angelo, Edificio G, Via Cinthia, I-80126, Napoli, Italy
[53] Wits Centre for Astrophysics, University of the Witwatersrand, 1 Jan Smuts Avenue, Braamfontein, Johannesburg 2050, South Africa
[54] Department of Physics, University of Pretoria, Hatfield, Pretoria 0028, South Africa
[55] Centre for Radio Astronomy Techniques and Technologies, Department of Physics and Electronics, Rhodes University, Makhanda 6140, South Africa
[56] JILA and Department of Astrophysical and Planetary Sciences, University of Colorado, Boulder, CO 80309, USA
[57] Tsung-Dao Lee Institute, Shanghai Jiao Tong University, Shengrong Road 520, Shanghai, 201210, People's Republic of China
[58] Las Cumbres Observatory, 6740 Cortona Drive, Suite 102, Goleta, CA 93117-5575, USA
[59] Department of Physics, University of California, Santa Barbara, CA 93106-9530, USA
[60] National Radio Astronomy Observatory, 520 Edgemont Road, Charlottesville, VA 22903, USA
[61] Department of Electrical Engineering and Computer Science, Massachusetts Institute of Technology, 32-D476, 77 Massachusetts Avenue, Cambridge, MA 02142, USA
[62] Google Research, 355 Main Street, Cambridge, MA 02142, USA
[63] Institut für Theoretische Physik und Astrophysik, Universität Würzburg, Emil-Fischer-Str. 31, D-97074 Würzburg, Germany
[64] Department of History of Science, Harvard University, Cambridge, MA 02138, USA
[65] Department of Physics, Harvard University, Cambridge, MA 02138, USA
[66] Dipartimento di Fisica, Università degli Studi di Cagliari, SP Monserrato-Sestu km 0.7, I-09042 Monserrato (CA), Italy
[67] INAF - Osservatorio Astronomico di Cagliari, via della Scienza 5, I-09047 Selargius (CA), Italy
[68] INFN, sezione di Cagliari, I-09042 Monserrato (CA), Italy
[69] Institute for Mathematics and Interdisciplinary Center for Scientific Computing, Heidelberg University, Im Neuenheimer Feld 205, Heidelberg 69120, Germany
[70] Institut für Theoretische Physik, Universität Heidelberg, Philosophenweg 16, 69120 Heidelberg, Germany
[71] CP3-Origins, University of Southern Denmark, Campusvej 55, DK-5230 Odense, Denmark
[72] Instituto Nacional de Astrofísica, Óptica y Electrónica. Apartado Postal 51 y 216, 72000. Puebla Pue., Mexico

[73] Consejo Nacional de Humanidades, Ciencia y Tecnología, Av. Insurgentes Sur 1582, 03940, Ciudad de México, Mexico
[74] Key Laboratory for Research in Galaxies and Cosmology, Chinese Academy of Sciences, Shanghai 200030, People's Republic of China
[75] Graduate School of Science, Nagoya City University, Yamanohata 1, Mizuho-cho, Mizuho-ku, Nagoya, 467-8501, Aichi, Japan
[76] Mizusawa VLBI Observatory, National Astronomical Observatory of Japan, 2-12 Hoshigaoka, Mizusawa, Oshu, Iwate 023-0861, Japan
[77] Department of Physics, McGill University, 3600 rue University, Montréal, QC H3A 2T8, Canada
[78] Trottier Space Institute at McGill, 3550 rue University, Montréal, QC H3A 2A7, Canada
[79] NOVA Sub-mm Instrumentation Group, Kapteyn Astronomical Institute, University of Groningen, Landleven 12, 9747 AD Groningen, The Netherlands
[80] Department of Astronomy, School of Physics, Peking University, Beijing 100871, People's Republic of China
[81] Kavli Institute for Astronomy and Astrophysics, Peking University, Beijing 100871, People's Republic of China
[82] Department of Astronomical Science, The Graduate University for Advanced Studies (SOKENDAI), 2-21-1 Osawa, Mitaka, Tokyo 181-8588, Japan
[83] Department of Astronomy, Graduate School of Science, The University of Tokyo, 7-3-1 Hongo, Bunkyo-ku, Tokyo 113-0033, Japan
[84] The Institute of Statistical Mathematics, 10-3 Midori-cho, Tachikawa, Tokyo, 190-8562, Japan
[85] Department of Statistical Science, The Graduate University for Advanced Studies (SOKENDAI), 10-3 Midori-cho, Tachikawa, Tokyo 190-8562, Japan
[86] Kavli Institute for the Physics and Mathematics of the Universe, The University of Tokyo, 5-1-5 Kashiwanoha, Kashiwa, 277-8583, Japan
[87] Leiden Observatory, Leiden University, Postbus 2300, 9513 RA Leiden, The Netherlands
[88] ASTRAVEO LLC, PO Box 1668, Gloucester, MA 01931, USA
[89] Applied Materials Inc., 35 Dory Road, Gloucester, MA 01930, USA
[90] Finnish Centre for Astronomy with ESO, University of Turku, FI-20014 Turun Yliopisto, Finland
[91] Aalto University Metsähovi Radio Observatory, Metsähovintie 114, FI-02540 Kylmälä, Finland
[92] Institute for Astrophysical Research, Boston University, 725 Commonwealth Avenue, Boston, MA 02215, USA
[93] University of Science and Technology, Gajeong-ro 217, Yuseong-gu, Daejeon 34113, Republic of Korea
[94] National Institute of Technology, Ichinoseki College, Takanashi, Hagisho, Ichinoseki, Iwate, 021-8511, Japan
[95] Joint Institute for VLBI ERIC (JIVE), Oude Hoogeveensedijk 4, 7991 PD Dwingeloo, The Netherlands
[96] CSIRO, Space and Astronomy, PO Box 76, Epping, NSW 1710, Australia
[97] Department of Physics, Ulsan National Institute of Science and Technology (UNIST), Ulsan 44919, Republic of Korea
[98] Department of Physics, Korea Advanced Institute of Science and Technology (KAIST), 291 Daehak-ro, Yuseong-gu, Daejeon 34141, Republic of Korea
[99] Kogakuin University of Technology & Engineering, Academic Support Center, 2665-1 Nakano, Hachioji, Tokyo 192-0015, Japan
[100] Graduate School of Science and Technology, Niigata University, 8050 Ikarashi 2-no-cho, Nishi-ku, Niigata 950-2181, Japan
[101] Physics Department, National Sun Yat-Sen University, No. 70, Lien-Hai Road, Kaosiung City 80424, Taiwan, R.O.C.
[102] Department of Astronomy, Kyungpook National University, 80 Daehak-ro, Buk-gu, Daegu 41566, Republic of Korea
[103] School of Astronomy and Space Science, Nanjing University, Nanjing 210023, People's Republic of China
[104] Key Laboratory of Modern Astronomy and Astrophysics, Nanjing University, Nanjing 210023, People's Republic of China
[105] INAF-Istituto di Radioastronomia, Via P. Gobetti 101, I-40129 Bologna, Italy
[106] Common Crawl Foundation, 9663 Santa Monica Boulevard 425, Beverly Hills, CA 90210, USA
[107] Instituto de Física, Pontificia Universidad Católica de Valparaíso, Casilla 4059, Valparaíso, Chile
[108] INAF-Istituto di Radioastronomia & Italian ALMA Regional Centre, Via P. Gobetti 101, I-40129 Bologna, Italy
[109] Department of Physics, National Taiwan University, No. 1, Sec. 4, Roosevelt Road, Taipei 106216, Taiwan, R.O.C.
[110] Instituto de Radioastronomía y Astrofísica, Universidad Nacional Autónoma de México, Morelia 58089, Mexico
[111] David Rockefeller Center for Latin American Studies, Harvard University, 1730 Cambridge Street, Cambridge, MA 02138, USA
[112] Yunnan Observatories, Chinese Academy of Sciences, 650011, Kunming, Yunnan Province, People's Republic of China
[113] Center for Astronomical Mega-Science, Chinese Academy of Sciences, 20A Datun Road, Chaoyang District, Beijing, 100012, People's Republic of China
[114] Key Laboratory for the Structure and Evolution of Celestial Objects, Chinese Academy of Sciences, 650011, Kunming, People's Republic of China
[115] Anton Pannekoek Institute for Astronomy, University of Amsterdam, Science Park 904, 1098 XH, Amsterdam, The Netherlands
[116] Gravitation and Astroparticle Physics Amsterdam (GRAPPA) Institute, University of Amsterdam, Science Park 904, 1098 XH Amsterdam, The Netherlands
[117] Center for Gravitation, Cosmology and Astrophysics, Department of Physics, University of Wisconsin-Milwaukee, P.O. Box 413, Milwaukee, WI 53201, USA
[118] Joint ALMA Observatory, Alonso de Córdova 3107, Vitacura 763-0355, Santiago, Chile
[119] European Southern Observatory, Alonso de Córdova 3107, Vitacura, Casilla 19001, Santiago, Chile
[120] School of Physics and Astronomy, Shanghai Jiao Tong University, 800 Dongchuan Road, Shanghai, 200240, People's Republic of China
[121] SCOPIA Research Group, University of the Balearic Islands, Dept. of Mathematics and Computer Science, Ctra. Valldemossa, Km 7.5, Palma 07122, Spain
[122] Artificial Intelligence Research Institute of the Balearic Islands (IAIB), Palma 07122, Spain
[123] Institut de Radioastronomie Millimétrique (IRAM), Avenida Divina Pastora 7, Local 20, E-18012, Granada, Spain
[124] National Institute of Technology, Hachinohe College, 16-1 Uwanotai, Tamonoki, Hachinohe City, Aomori 039-1192, Japan
[125] Research Center for Astronomy, Academy of Athens, Soranou Efessiou 4, 115 27 Athens, Greece
[126] Department of Physics, Villanova University, 800 Lancaster Avenue, Villanova, PA 19085, USA
[127] Physics Department, Washington University, CB 1105, St. Louis, MO 63130, USA
[128] Departamento de Matemática da Universidade de Aveiro and Centre for Research and Development in Mathematics and Applications (CIDMA), Campus de Santiago, 3810-193 Aveiro, Portugal
[129] School of Physics, Georgia Institute of Technology, 837 State St NW, Atlanta, GA 30332, USA
[130] School of Space Research, Kyung Hee University, 1732, Deogyeong-daero, Giheung-gu, Yongin-si, Gyeonggi-do 17104, Republic of Korea
[131] Canadian Institute for Theoretical Astrophysics, University of Toronto, 60 St. George Street, Toronto, ON M5S 3H8, Canada
[132] Dunlap Institute for Astronomy and Astrophysics, University of Toronto, 50 St. George Street, Toronto, ON M5S 3H4, Canada
[133] Canadian Institute for Advanced Research, 180 Dundas St West, Toronto, ON M5G 1Z8, Canada
[134] Dipartimento di Fisica, Università di Trieste, I-34127 Trieste, Italy
[135] INFN Sez. di Trieste, I-34127 Trieste, Italy
[136] Department of Physics, National Taiwan Normal University, No. 88, Sec. 4, Tingzhou Road, Taipei 116, Taiwan, R.O.C.
[137] Center of Astronomy and Gravitation, National Taiwan Normal University, No. 88, Sec. 4, Tingzhou Road, Taipei 116, Taiwan, R.O.C.
[138] Signal Processing Research Centre, Tampere University, FI-33720 Tampere, Finland
[139] Gemini Observatory/NSF NOIRLab, 670 N. A'ohōkū Place, Hilo, HI 96720, USA
[140] Frankfurt Institute for Advanced Studies, Ruth-Moufang-Strasse 1, D-60438 Frankfurt, Germany
[141] School of Mathematics, Trinity College, Dublin 2, Ireland
[142] Julius-Maximilians-Universität Würzburg, Fakultät für Physik und Astronomie, Institut für Theoretische Physik und Astrophysik, Lehrstuhl für Astronomie, Emil-Fischer-Str. 31, D-97074 Würzburg, Germany
[143] Department of Physics, University of Toronto, 60 St. George Street, Toronto, ON M5S 1A7, Canada
[144] Department of Physics, Tokyo Institute of Technology, 2-12-1 Ookayama, Meguro-ku, Tokyo 152-8551, Japan
[145] Hiroshima Astrophysical Science Center, Hiroshima University, 1-3-1 Kagamiyama, Higashi-Hiroshima, Hiroshima 739-8526, Japan
[146] Aalto University Department of Electronics and Nanoengineering, PL 15500, FI-00076 Aalto, Finland

[147] Institut de Radioastronomie Millimétrique (IRAM), 300 rue de la Piscine, F-38406 Saint Martin d'Hères, France
[148] Jeremiah Horrocks Institute, University of Lancashire, Preston PR1 2HE, UK
[149] National Biomedical Imaging Center, Peking University, Beijing 100871, People's Republic of China
[150] College of Future Technology, Peking University, Beijing 100871, People's Republic of China
[151] Department of Physics and Astronomy, University of Lethbridge, Lethbridge, Alberta T1K 3M4, Canada
[152] Netherlands Organisation for Scientific Research (NWO), Postbus 93138, 2509 AC Den Haag, The Netherlands
[153] Frontier Research Institute for Interdisciplinary Sciences, Tohoku University, Sendai 980-8578, Japan
[154] Astronomical Institute, Tohoku University, Sendai 980-8578, Japan
[155] Department of Physics and Astronomy, Seoul National University, Gwanak-gu, Seoul 08826, Republic of Korea
[156] SNU Astronomy Research Center, Seoul National University, Gwanak-gu, Seoul 08826, Republic of Korea
[157] Department of Astronomy, University of Illinois at Urbana-Champaign, 1002 West Green Street, Urbana, IL 61801, USA
[158] ASTRON, Oude Hoogeveensedijk 4, 7991 PD Dwingeloo, The Netherlands
[159] University of New Mexico, Department of Physics and Astronomy, Albuquerque, NM 87131, USA
[160] Centre for Mathematical Plasma Astrophysics, Department of Mathematics, KU Leuven, Celestijnenlaan 200B, B-3001 Leuven, Belgium
[161] Physics Department, Brandeis University, 415 South Street, Waltham, MA 02453, USA
[162] Tuorla Observatory, Department of Physics and Astronomy, University of Turku, FI-20014 Turun Yliopisto, Finland
[163] Radboud Excellence Fellow of Radboud University, Nijmegen, The Netherlands
[164] School of Natural Sciences, Institute for Advanced Study, 1 Einstein Drive, Princeton, NJ 08540, USA
[165] School of Physics, Huazhong University of Science and Technology, Wuhan, Hubei, 430074, People's Republic of China
[166] Mullard Space Science Laboratory, University College London, Holmbury St. Mary, Dorking, Surrey, RH5 6NT, UK
[167] Center for Astronomy and Astrophysics and Department of Physics, Fudan University, Shanghai 200438, People's Republic of China
[168] Astronomy Department, University of Science and Technology of China, Hefei 230026, People's Republic of China
[169] Department of Physics and Astronomy, Michigan State University, 567 Wilson Road, East Lansing, MI 48824, USA
Received 2025 September 9; revised 2025 December 21; accepted 2025 December 22; published 2026 March 25

Abstract

Event Horizon Telescope (EHT) images of the supermassive black hole M87* depict an asymmetric ring of emission. General relativistic magnetohydrodynamic (GRMHD) models of M87* and its accretion disk predict that the amplitude and location of the ring's peak brightness asymmetry should fluctuate due to turbulence in the source plasma. We compare the observed distribution of brightness asymmetry amplitudes to the simulated distribution in GRMHD models, across varying black hole spin a_*. We show that, for strongly magnetized (MAD) models, three epochs of EHT data marginally disfavor $|a_*| \lesssim 0.2$. This is consistent with the Blandford–Znajek model for M87's jet, which predicts that M87* should have nonzero spin. We show quantitatively how future observations could improve spin constraints and discuss how improved spin constraints could distinguish between differing jet-launching mechanisms and black hole growth scenarios.

Unified Astronomy Thesaurus concepts: Supermassive black holes (1663); Accretion (14); Low-luminosity active galactic nuclei (2033); Magnetohydrodynamics (1964); Radiative transfer (1335); Very long baseline interferometry (1769)

Materials only available in the online version of record: machine-readable table

1. Introduction

The Event Horizon Telescope (EHT) has captured images of the supermassive black hole M87* (Event Horizon Telescope Collaboration et al. 2019a, 2024, 2025b), at the center of the M87 galaxy. These images feature a bright ring-like structure (the "ring") that encloses a dark low-intensity region (the "shadow"). The ring is produced by synchrotron emission from hot plasma located within a few Schwarzschild radii of the black hole. The shadow corresponds to the region where the observer's line of sight intersects the event horizon. The ring diameter is consistent with a black hole of mass $M = 6.5 \times 10^9 M_\odot$ located at a distance $D = 16.8$ Mpc from Earth (Event Horizon Telescope Collaboration et al. 2019f), in agreement with stellar kinematics measurements (K. Gebhardt et al. 2011; E. R. Liepold et al. 2023). The ring has a north–south brightness asymmetry, with the brightness peak shifting to the southwest in recent observations (Event Horizon Telescope Collaboration et al. 2024, 2025b).

In this paper, we study how ring brightness asymmetry constrains dimensionless black hole spin: $a_* \equiv Jc/GM^2$ for black hole angular momentum J, speed of light c, and gravitational constant G. The task of recovering robust spin measurements for supermassive black holes is a long-standing problem in the field. From a theoretical perspective, spin and mass are the two quantities that completely define the spacetime geometry of any uncharged black hole (R. P. Kerr 1963). In the astrophysical context, spin can be used to discriminate different scenarios of black hole formation and growth (e.g., A. Merloni & S. Heinz 2008; C. Bambi et al. 2021; C. S. Reynolds 2021; A. Ricarte et al. 2023). Tilt between the spin axis and the accretion disk angular momentum axis can lead to Lense–Thirring precession of the disk and jet (e.g., J. M. Bardeen & J. A. Petterson 1975; P. C. Fragile & P. Anninos 2005; P. C. Fragile et al. 2007; H. Shiokawa 2013; M. Liska et al. 2018). Spin is also predicted to affect orbits of stars passing close to the black hole via Lense–Thirring precession (Y. Levin & A. M. Beloborodov 2003) and resonant friction (Y. Levin 2024) effects. It can even be used to constrain merger history and cosmological formation of the host galaxy

[170] Deceased.
[171] Corresponding author.

(e.g., C. F. Gammie et al. 2004; A. Ricarte et al. 2023, 2025; L. Sala et al. 2024).

Determining spins of supermassive black holes is especially important for understanding jet formation. To this day, the physical mechanism of jet launching has not been confirmed. The Blandford–Znajek mechanism (R. D. Blandford & R. L. Znajek 1977), which is the leading model for jet formation, predicts that jets are powered by frame dragging of magnetic field lines that thread the horizon of a spinning black hole. The extraction of black hole spin energy powers the jet. There are alternatives, however. One of the most prominent competing models is the Blandford–Payne mechanism (R. D. Blandford & D. G. Payne 1982), in which accretion disk rotation powers the jet. Other models suggest gas, radiation (M. J. Rees et al. 1981), and magnetic field (D. Lynden-Bell & C. Boily 1994) pressures as alternative driving mechanisms. These models predict different probability distributions for the spin based on the presence of a jet with a given power. They likewise predict different equilibrium values for spin over cosmic time. Therefore, precise measurement of spin is important for determining the correct model of jet launching. Such an analysis is relevant for both M87*, where the jet feature is prominent (see, e.g., R. C. Walker et al. 2018), and Sgr A*, where the presence of a jet is still debated.

As of now, spin remains elusive. Current spin constraints rely on X-ray techniques that apply only to high accretion rate systems ($0.01 \lesssim \dot{M}/\dot{M}_{\rm Edd} \lesssim 0.3$, per C. S. Reynolds 2021; C. Bambi et al. 2021). No observational spin constraints exist for lower accretion black holes ($\dot{M}/\dot{M}_{\rm Edd} < 0.01$), which are far more prevalent in the local Universe (A. Merloni & S. Heinz 2008; although many theoretical studies of spin evolution in these systems have been made, including F. Pacucci & A. Loeb 2020; A. Ricarte et al. 2023; L. Sala et al. 2024). The spin of Sgr A* in our own galactic center, for example, is a topic of current research.

For M87*, there is currently no direct, statistically significant spin constraint. Indirect spin constraints have been made via the jet power, favoring $|a_*| > 0$ (e.g., R. Nemmen 2019; Event Horizon Telescope Collaboration et al. 2019e). This analysis, however, relies on highly uncertain observational constraints, assumes a Blandford–Znajek powered jet, and depends on jet launching at an earlier time. This motivates a conservative approach for GRMHD model-dependent spin constraints with jet power (Event Horizon Telescope Collaboration et al. 2019e). Near-horizon electric vector polarization angles also marginally favor retrograde spins, where the accretion angular momentum vector and the black hole spin vector are antialigned (D. C. M. Palumbo et al. 2020; Event Horizon Telescope Collaboration et al. 2021, 2025a; M. Janssen et al. 2025). However, uncertainties in interpreting polarization data (due to, e.g., Faraday rotation and year-to-year variability) motivate complementary constraints using near-horizon total intensity data.

Here, we constrain spin by comparing a particular measure of the brightness asymmetry magnitude (using the amplitude of the fitted $m = 1$ m-ring) in EHT observations of M87* with the same measure in a library of synthetic data based on GRMHD simulations. Our library—the "Illinois v5" KHARMA library—contains models with a dense distribution of spins and parameterized electron distribution functions. The observational data were obtained by the EHT Collaboration during the 2017, 2018, and 2021 observing campaigns (hereafter EHTC M87 I-VI for Event Horizon Telescope Collaboration et al. 2019a, 2019b, 2019c, 2019d, 2019e, 2019f; EHTC M87 2018 I-II for Event Horizon Telescope Collaboration et al. 2024, 2025a; and EHTC M87 2021 for Event Horizon Telescope Collaboration et al. 2025b). Reconstructed EHT images from all three years are shown in Figure 1.

The observed ring in Figure 1 has a brightness asymmetry. Earlier studies of asymmetry in M87* have considered its dependence on the black hole inclination (see L. Medeiros et al. 2022) and compared it to the ring asymmetry of Sgr A* (see J. C. Faggert et al. 2025). The brightness asymmetry is produced by a complicated interplay of Doppler boosting, gravitational lensing, frame dragging, radiative transfer effects, and gravitational redshift (EHTC M87 V), which can depend on spin. It is possible, therefore, that there exists a correlation between the asymmetry magnitude and the spin of the black hole. This paper investigates that correlation using GRMHD models.

The paper is structured as follows. In Section 2, we describe a strongly magnetized (MAD) model library. Section 3 discusses how brightness asymmetry is estimated from the data and from synthetic images. In Section 4, we present the distribution of asymmetry across spin. We then discuss in Section 5, including a comparison with earlier work (Section 5.1), an analysis of future observations (Section 5.2), a discussion of limitations (Sections 5.3–5.4), and a proposed test of the Blandford–Znajek mechanism (Section 5.5). Finally, we summarize in Section 6. In the Appendix, we investigate the distribution of asymmetries in weakly magnetized (SANE) models and prior GRMHD models (Appendix A), demonstrate that our spin constraints are insensitive to methodology changes (Appendix B), and present fits to the distribution of asymmetry in all models (Appendix C).

2. Models

To assess the probability of different spins producing the observed asymmetry, we compare EHT data to a library of synthetic data based on GRMHD models, which span a range of model parameters.

The library was produced using the `PATOKA` pipeline (G. N. Wong et al. 2022), which models the accretion flow using ideal general relativistic magnetohydrodynamics (GRMHD) simulations and then ray-traces GRMHD snapshots to produce synthetic images. The GRMHD simulations are integrated with the KHARMA code (B. S. Prather 2024), and the synthetic images are produced using `ipole` (M. Mościbrodzka & C. F. Gammie 2018). For this study, we use the "v5" version of the Illinois GRMHD library (N. J. Bowden et al. 2026, in preparation). Results from the v3 library (V. Dhruv et al. 2025), which were produced with an outdated adiabatic index among other differences, used the `iharm` code (B. Prather et al. 2021) and are described in Appendix A.

Our GRMHD simulations are a natural progression of the radiatively inefficient accretion flow (RIAF) model (S. Ichimaru 1977; R. Narayan & I. Yi 1994; R. Narayan et al. 1995; E. Quataert & R. Narayan 1999; F. Yuan et al. 2003). These accretion disks are typically optically thin and geometrically thick, comprised of relativistically hot plasma (M. J. Rees et al. 1982; R. Narayan & I. Yi 1995; R. Narayan et al. 1995;

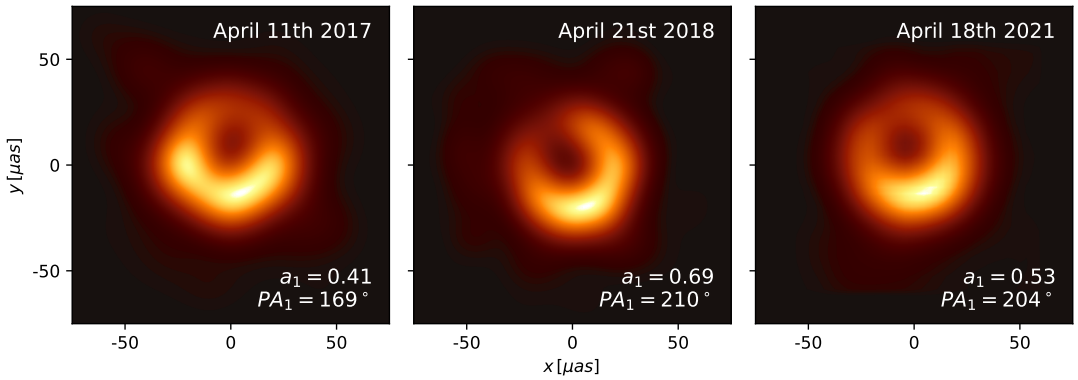

Figure 1. EHT images of M87* on 2017 April 11 (EHTC M87 I, left), 2018 April 21 (EHTC M87 2018 I, middle), and 2021 April 18 (EHTC M87 2021, right). All images show a brightness asymmetry with a peak magnitude in the south. The asymmetry magnitude a_1 and angle PA_1 measured in this work are shown.

C. S. Reynolds et al. 1996; F. Yuan et al. 2002; T. Di Matteo et al. 2003; F. Yuan & R. Narayan 2014). This model is well-supported by observations, which find that M87 has a relatively low-luminosity active galactic nuclei, suggesting that M87* has a low accretion rate (e.g., F. Yuan & R. Narayan 2014). The RIAF thick-disk model is also supported by EHT observations (EHTC M87 V). See G. N. Wong et al. (2022) for additional discussion.

Our GRMHD fluid simulations have two parameters: accretion state and black hole spin. The accretion state typically falls into strongly or weakly magnetized modes (MAD or SANE). Magnetically arrested disk (MAD) models (I. V. Igumenshchev et al. 2003; R. Narayan et al. 2003; A. Tchekhovskoy et al. 2011) have near-horizon magnetic fields that are strong enough to impede accretion. This limits the magnetic flux on the horizon to a characteristic value that depends on the accretion rate. Standard and normal evolution (SANE) models (R. Narayan et al. 2012; A. Sądowski et al. 2013) have weaker near-horizon fields and are more similar to classical thin disks, although they are optically thin and geometrically thick. In the main text, we focus on MAD models. This is motivated by evidence that MAD models are favored by M87* data, as they are more likely to pass jet power and polarization constraints (EHTC M87 V; EHTC M87 IX). For v5, we densely sample the dimensionless spin a_* in 13 steps, ranging from -0.97 to 0.97 (N. J. Bowden et al. 2026, in preparation). Recall that for a Kerr black hole, $a_* \in [-1, 1]$. Here, positive spin means the accretion disk angular momentum vector is prograde (aligned) with respect to black hole spin vector, while negative spin means that the accretion disk angular momentum vector is retrograde (antialigned). The spin and accretion disk angular momentum vector are assumed to be coaxial: we do not consider tilted disks. Our analysis therefore uses 13 MAD GRMHD fluid simulations.

The radiative transfer step has three parameters: inclination, $R_{\rm high}$, and $R_{\rm low}$.

The inclination i is the angle between the accretion flow orbital angular momentum vector and the line of sight. We assume that the black hole spin vector, the accretion flow orbital angular momentum vector, and the large-scale jet are coaxial and that the approaching jet inclination is 17° (see, e.g., R. C. Walker et al. 2018). The position angle of the brightest point on the ring is known to depend on spin, and the position angle of the observed asymmetry implies that the spin vector is pointed away from Earth (EHTC M87 V). Adopting this constraint, we set $i = 17^\circ$ for $a_* < 0$ and $i = 163^\circ$ for $a_* \geqslant 0$. The different inclination angle for positive and negative spins has no impact on the asymmetry magnitude distribution.

Table 1
Model Parameters

Parameter	Sampled Values
Magnetic Flux Mode	MAD
Spin	0, ±0.25, ±0.5, ±0.75, ±0.85, ±0.9375, ±0.97
$R_{\rm high}$	10, 40, 80, 160
$R_{\rm low}$	1, 10
i [deg]	17° (for $a_* < 0$), 163° (for $a_* \geqslant 0$)

Note. v5 model parameters used for the analysis. Each combination of parameter values corresponds to one model. SANE models are discussed in Appendix A.

The radiative properties of the plasma depend on the electron distribution function, which is not determined by the GRMHD simulations. We use a model with parameters $R_{\rm high}$ and $R_{\rm low}$ to assign a distribution function to the electrons. The model assumes that (1) the electrons are thermal at temperature T_e; (2) the ions are thermal at temperature T_i; (3) T_i can be deduced directly from the simulation; and (4) T_i/T_e depends only on the local, instantaneous value of the plasma $\beta \equiv P_{\rm gas}/P_{\rm mag}$ for gas pressure $P_{\rm gas}$ and magnetic pressure $P_{\rm mag}$. Then, following M. Mościbrodzka et al. (2016),

$$\frac{T_i}{T_e} = R_{\rm high}\frac{\tilde{\beta}^2}{1+\tilde{\beta}^2} + R_{\rm low}\frac{1}{1+\tilde{\beta}^2} \quad (1)$$

for $\tilde{\beta} = \beta/\beta_{\rm crit}$ and $\beta_{\rm crit} = 1$. $R_{\rm high}$ and $R_{\rm low}$ are thus dimensionless temperature ratios. $R_{\rm low}$ dominates at low $\tilde{\beta}$ and $R_{\rm high}$ at high $\tilde{\beta}$. We consider models with $R_{\rm high} = 10, 40, 80, 160$ and $R_{\rm low} = 1, 10$ (EHTC M87 V; EHTC M87 VIII). We do not consider $R_{\rm high} = 1$ because it is disfavored by the data (EHTC M87 V; EHTC M87 IX; EHTC M87 2018 II). There are thus eight unique combinations of i, $R_{\rm high}$, and $R_{\rm low}$.

Model parameters are listed in Table 1. Each of 104 PATOKA models contains 6000 images, produced at $5\,t_g$ cadence (for gravitational time $t_g \equiv GMc^{-3}$) in the interval from time $20{,}000\,t_g$ to $50{,}000\,t_g$ after the start of the simulation. Time-averaged images for different spins are shown in Figure 2 for both MAD and SANE models. It is clear from the figure that ring asymmetry and position angle are correlated with spin: as the magnitude of spin increases, the

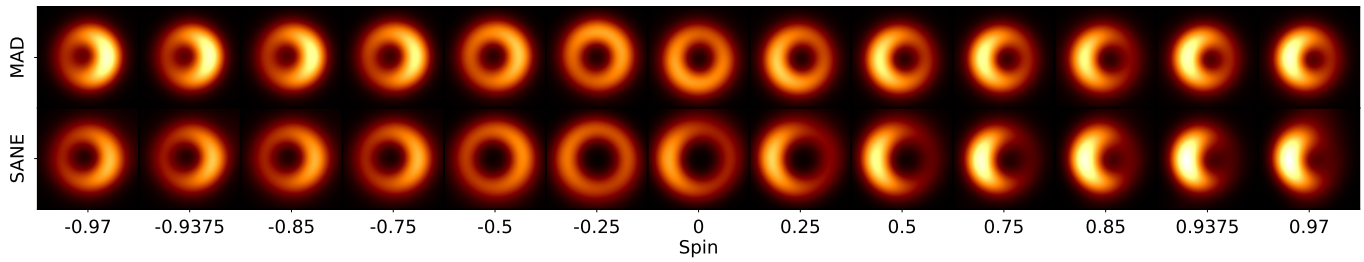

Figure 2. Mean images for all models in the v5 library (averaging over $R_{\rm high}$, $R_{\rm low}$, and time, and blurred using a 15 μas full width at half maximum Gaussian kernel) at $i = 17°$ for $a_* < 0$ and $i = 163°$ for $a_* \geqslant 0$, across each spin (columns) for MADs (top row) and SANEs (bottom row). Asymmetry magnitude typically increases with $|a_*|$. In these images, the projected prograde spins point up, retrograde spins point down, the accretion flow angular momentum points up, and jet axis is vertical. The position angle of the brightness asymmetry approximately follows the sign of the spin, consistent with EHTC M87 V. See Appendix A for a discussion of SANEs.

magnitude of the brightness asymmetry generally also increases.

A comparison of MAD and SANE models in our main v5 library and in the v3 library, which is run with different physical assumptions and a different GRMHD code, is discussed in Appendix A. We prefer v5 models because (1) they are run at higher resolution; (2) they are run longer and therefore provide better sampling of the asymmetry distribution; (3) they sample spin more densely (13 spins in v5 versus 5 spins in v3); and (4) v5 uses adiabatic index $\gamma = 5/3$, while v3 uses $\gamma = 4/3$. If $T_e \ll T_i$, then the gas pressure is dominated by the ions, which are nonrelativistic, and thus $\gamma = 5/3$ is more appropriate (for a discussion, see C. F. Gammie 2025). In the following section, we discuss how we measure asymmetry in models and observational data.

3. Measuring Asymmetry

3.1. EHT Observations

Very-long-baseline interferometry (VLBI) arrays such as the EHT sample the (u, v), or Fourier, domain. The sampling is based on the coverage of their baselines projected onto the sky. To measure ring asymmetry with (u, v) data, we fit a parameterized m-ring model using the Comrade package for Bayesian modeling of VLBI observations (P. Tiede 2022). We demonstrate consistency with asymmetry fits in the image domain using variational image domain analysis (VIDA; P. Tiede et al. 2022) in Section 3.2. Detailed validation of the parameter optimization method is described in P. Tiede et al. (2022).

Our parameterized Comrade model has two components: a ring with intensity $I_{\rm ring}$ and a Gaussian background component with intensity $I_{\rm bg}$. The total intensity is $I = I_{\rm ring} + I_{\rm bg}$. The Gaussian background intensity is

$$I_{bg}(x, y) \propto (1 - f)\exp\left(-\frac{(x')^2}{2\sigma_g^2} - \frac{(y')^2}{2\sigma_g^2(1 + \tau_g)^2}\right) \quad (2)$$

for $x' = (x - x_g)\cos\xi_g + (y - y_g)\sin\xi_g$ and $y' = -(x - x_g)\cos\xi_g + (y - y_g)\sin\xi_g$. The Gaussian is scaled by $(1 - f)$ with standard deviation σ_g, given ellipticity τ_g, rotated by angle ξ_g, and shifted by (x_g, y_g). The background component thus has six parameters (these parameters are unitless, as the fitting is done to normalized images; the images can be rescaled after fitting as needed). This Gaussian background component is typical for modeling EHT data (P. Tiede et al. 2022; EHTC M87 2018 II). The ring intensity is modeled with a so-called $m = 4$ m-ring:

$$I_{\rm ring}(r, \theta) \propto \left[1 - \sum_{m=1}^{4} a_m \cos(m\theta - {\rm PA}_m)\right] \exp\left(-\frac{(r - r_0)^2}{2\sigma^2}\right). \quad (3)$$

The m-ring is a Fourier series wrapped along a ring of Gaussian thickness (M. D. Johnson et al. 2020; P. Tiede et al. 2022). We truncate the Fourier series at $m = 4$ (which is typically sufficient to describe EHT sources; EHTC M87 2018 I) and require that $a_m < 1$ to ensure positive intensity everywhere. Our $m = 4$ m-ring has 10 parameters: ring radius r_0, ring thickness σ, amplitudes a_m, and position angles ${\rm PA}_m$ for $m = 1$ through 4. Here, a_1 captures the large-scale brightness asymmetry, while a_2 through a_4 capture smaller scale turbulent structure. We use a_1, the normalized amplitude of the $m = 1$ Fourier component, as our measure of ring brightness asymmetry. In our convention, notice that a ring with $a_1 = 0$ is symmetric, while a ring with $a_1 = 1$ has an amplitude as large as its mean.

The model parameters are adjusted by the Comrade optimizers to fit EHT visibility amplitude and closure phase data. Using this procedure to model EHT 2017, 2018, and 2021 observations (EHTC M87 I; EHTC M87 2018 I; EHTC M87 2021) yields $a_1 = 0.41 \pm 0.04$, $a_1 = 0.69 \pm 0.10$, and $a_1 = 0.53 \pm 0.04$, respectively. We use a different measure of asymmetry than EHTC M87 IV, EHTC M87 2018 I, and EHTC M87 2021, and therefore the asymmetries reported here differ from prior values reported by EHT (See Section 5.1). The quality of fit can be assessed using the mean squared standardized residual χ^2, normalized by the number of data points. The normalized χ^2 is 1.9, 0.9, and 2.6 in 2017, 2018, and 2021, respectively (note these are not reduced χ^2 values). For additional discussion, see EHTC M87 IV, P. Tiede (2022), and EHTC M87 2018 I, which finds that an $m = 4$ m-ring has among the highest Bayesian evidence when fitting to EHT data in a survey of 25 geometric modeling templates. Our results are insensitive to changes in the m-ring modeling template, as described in Appendix B.

3.2. Simulated Images

We apply the same analysis technique to our synthetic data as we did to the real data. Each GRMHD model contains a sequence of images separated by $5\,t_g$. The images are correlated on timescales $\sim 100\,t_g$, so we downsample to a cadence of $125\,t_g$ (see Section 5.2) to obtain independent

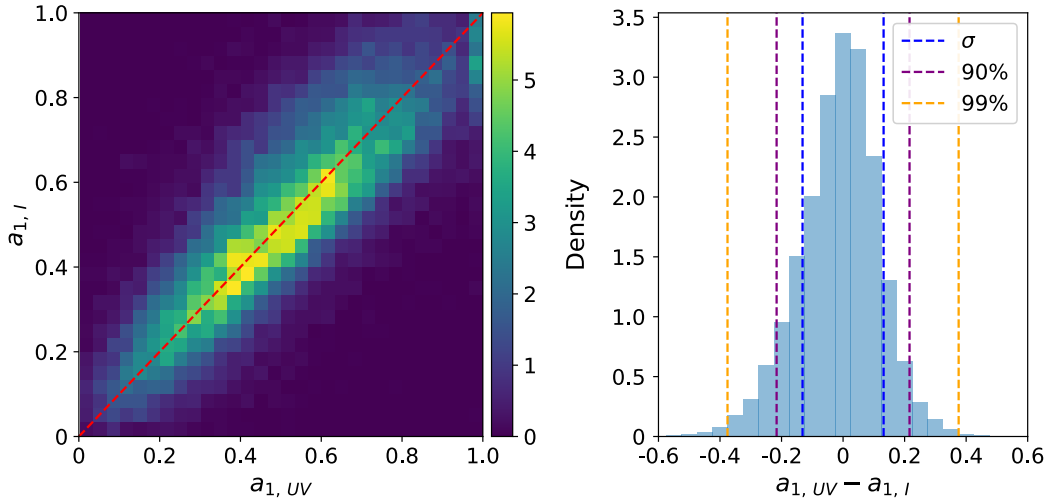

Figure 3. Comparison of the asymmetry magnitude measured in the image domain $a_{1,I}$ and (u, v) domain $a_{1,UV}$ for MAD models, plotted as the density of total snapshots. Left: the distribution of snapshots in $(a_{1,I}, a_{1,UV})$ space. The red line corresponding to $a_{1,I} = a_{1,UV}$. We set a ceiling of $a_{1,UV} \leqslant 1$ in the (u, v) optimizer, which accounts for the cluster of snapshots at $a_{1,UV} = 1$. These outlier values occur in <1% of total snapshots and do not affect our results (see Appendix B). Right: distribution of $a_{1,UV} - a_{1,I}$, with 1σ, 90%, and 99% boundaries marked. Nearly 90% of snapshots have $|a_{1,UV} - a_{1,I}| < 0.2$.

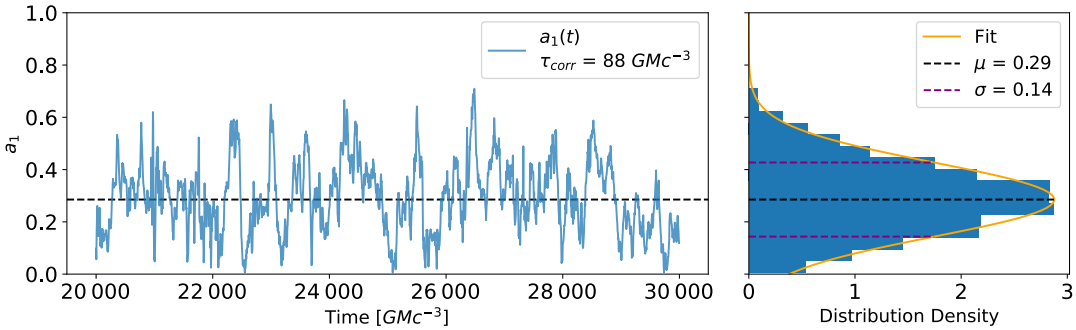

Figure 4. Left: evolution of asymmetry a_1 in time, over a 10,000 t_g time window, for the $a_* = 0$, $R_{\rm low} = 1$, $R_{\rm high} = 40$, MAD model. Right: the distribution of asymmetry amplitudes for this model window. The truncated Gaussian fit to the distribution is shown, with the mode $\mu = 0.29$ and standard deviation $\sigma = 0.14$.

synthetic observations. This leaves 240 images per unique combination of spin, $R_{\rm high}$, and $R_{\rm low}$, and 1920 unique images per unique spin.

To measure asymmetry in models, we require synthetic data generated with realistic observational conditions. We first rotate the ground truth images to match the large-scale jet axis expected from observations (again, we assume the large-scale jet, disk angular momentum vector, and black hole spin vector are coaxial). We generate (u, v) data by Fourier transforming our synthetic images, then sampling the resulting visibility amplitudes and closure phases using EHT (u, v) coverage, with realistic observational noise (including baseline-dependent thermal noise, generated using the eht-imaging software; A. A. Chael et al. 2018). Finally, we fit the m-ring model parameters to the resulting synthetic data using Comrade, as in Section 3.1. For simplicity, we assume 2018 EHT (u, v) coverage and conditions. The results are consistent if we use 2017 or 2021 (u, v) coverage and observational noise instead (see Appendix B), or fit directly in the image domain.

A comparison of asymmetry $a_{1,I}$ measured in the image domain to asymmetry $a_{1,UV}$ measured from synthetic (u, v) data shows the effect of limited (u, v) coverage. We have compared $a_{1,UV}$ and $a_{1,I}$ for all snapshots in the library. The results are shown in Figure 3. About 68% of snapshots have $|a_{1,UV} - a_{1,I}|$ less than 0.13, and 90% have difference less than 0.22. Furthermore, the root-mean squared difference is smaller than the variation of asymmetry in an individual model. Evidently $a_{1,UV}$ and $a_{1,I}$ are highly correlated and $a_{1,UV}$ provides a nearly unbiased estimate of $a_{1,I}$ (notice the minimal offset in Figure 3). A small fraction of snapshots cluster around $a_{1,UV} = 1$. This artifact occurs due to the chosen bounds and does not effect the results. We conclude that asymmetry can be accurately measured, even with EHT's limited (u, v) coverage.

The asymmetry fluctuates over time. Across the v5 model library, we find a mean correlation timescale for a_1 of $\tau_{\rm corr} \approx 70\, t_g$ for SANEs and $\tau_{\rm corr} \approx 115\, t_g$ for MADs. An example asymmetry evolution for a model with $a_* = 0$, $R_{\rm low} = 1$, and $R_{\rm high} = 40$ is shown in Figure 4. The asymmetry approximately follows a truncated normal distribution. For this example, the a_1 distribution has mode $\mu = 0.29$, standard deviation $\sigma \approx 0.14$, and correlation timescale $88\, t_g$.

4. Results

After measuring asymmetry for all MAD models, we find the asymmetry distributions show a clear spin dependence, consistent with Figure 2. Figure 5 shows the asymmetry distributions for MAD models, marginalizing over all parameters except spin. Models with zero spin show minimum asymmetry, while models with maximum spin magnitude have

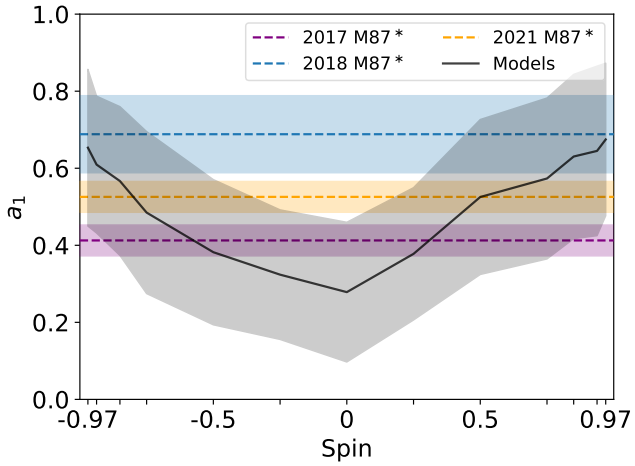

Figure 5. Distribution of MAD model asymmetry. The black line shows the modes μ of truncated Gaussians fitted to modeled asymmetry distributions, marginalizing over $R_{\rm high}$ and $R_{\rm low}$, at each spin. The gray band shows 1σ distribution variation. EHT measurements of asymmetry in M87* are shown as dashed lines, surrounded by 1σ regions (colored shaded bands). Spin values present in the models are shown with x-axis tick marks. The 2017, 2018, and 2021 data fall above the 50th percentile for zero-spin models. The 2018 asymmetry falls above the 90th percentile for zero-spin models.

mean asymmetry that is over twice as large. Truncated Gaussian fit parameters to these model distributions are provided in Table 2. Fits for SANE models are provided in Appendix C. We filter out all images with $a_1 > 0.99$ before fitting to improve accuracy. We note that observations are well below this threshold and that this process has no major effect on our statistical results (see Appendix B).

The figure also shows the observed asymmetries from 2017 to 2021. As above and in Figure 1, the measured asymmetry for 2017, 2018, and 2021 EHT data are 0.41, 0.69, and 0.53, respectively. The asymmetry is largest in 2018, when there appears to be the largest difference between the ring's brightness peak and brightness minimum. The 2021 image has a similar position angle, but has relatively more emission on the ring's dim side. 2017 has the least asymmetry, with a smaller difference between the ring's maximum and minimum brightness, and with a wider multimodal bright side. Our measured asymmetry values fit what is seen by-eye. In Figure 5, we see the 2018 asymmetry is above the 90th percentile of all nonspinning black hole models, while the 2017 and 2021 asymmetries lie above the 50th percentile of all nonspinning black hole models. The data clearly disfavor zero-spin models.

To assess the significance of the inconsistency between the data and the models, we use the Kolmogorov–Smirnov (KS) test. The KS test provides a probability p that the difference between the observed and model cumulative distributions are as large or larger than observed.

The probability for each spin, marginalizing over each model $R_{\rm high}$ and $R_{\rm low}$, are shown in Figure 6. There are two lines in the figure: one for the truncated Gaussian fit to the GRMHD asymmetry distribution (the "one-sample" KS test), and one using measured asymmetries of individual images drawn from each model (the "two-sample" KS test). Evidently the two are very close. Models with $a_* = 0$ and $a_* = -0.25$ give lower p-values than higher spin models: $a_* = 0$ models have $p = 0.026$ and $a_* = -0.25$ models have $p = 0.049$ in the two-sample KS test. Zero-spin models are strongly disfavored. Maximum p-values occur at $a_* = -0.75$, 0.5, and 0.75, as spins with larger magnitudes produce asymmetries that slightly exceed the current mean of observations. However, the relative difference in p between these highly spinning models is insignificant; all are consistent with the data at present. If the spin of M87* is nonzero and the models provide the correct asymmetry distributions, then future observations will soon tighten these constraints.

In the discussion above, we marginalize over all radiative transfer parameters $R_{\rm high}$ and $R_{\rm low}$ at each spin. Figure 7 shows KS test probabilities for $a_* = 0$ models broken out for different $R_{\rm high}$ and $R_{\rm low}$. Recall that these parameters set the ratio of electron temperature to ion temperature as a function of plasma β.

The asymmetry is only weakly dependent on $R_{\rm high}$ and $R_{\rm low}$ in MAD models. The emission region is relatively insensitive to $R_{\rm high}$ and $R_{\rm low}$ in MADs (EHTC M87 V; G. N. Wong et al. 2022), so the asymmetry's weak dependence on these parameters is expected. Still, the $R_{\rm low} = 1$ models tend to exhibit lower p than $R_{\rm low} = 10$ models. In Figure 7, we see this trend for $a_* = 0$, as $R_{\rm low} = 10$ models have slightly higher asymmetry than $R_{\rm low} = 1$, closer to observations. Prograde MAD $R_{\rm low} = 10$ models produce slightly less asymmetry than $R_{\rm low} = 1$, also closer to the observed mean. The $R_{\rm low} = 10$ models are also favored by polarized EHT data: they more frequently reproduce the observed polarization fraction and structure. Cooler electron temperatures are a plausible consequence of radiative cooling. Meanwhile, models with low $R_{\rm high}$ (e.g., $R_{\rm high} = 1$) are disfavored by other constraints: they overproduce X-rays, underproduce jet power, are too radiatively efficient (EHTC M87 V), and have a too high polarization fraction (EHTC M87 VIII; EHTC M87 IX). While our asymmetry does not exclude $R_{\rm high} = 10$, it does mildly favor $R_{\rm low} = 10$. It seems cooler electrons are preferred.

5. Discussion

The asymmetry in black hole images is determined by multiple physical processes (A. Chael et al. 2026, in preparation). These include Doppler beaming, gravitational lensing, and radiative transfer effects, e.g., the angle at which the line of sight passes through the midplane (lines of sight that are more nearly parallel to the midplane have higher opacity), and the angle between the magnetic field and the line of sight (lines of sight normal to the magnetic field have higher synchrotron opacity).

Doppler shift is an important contributor to the asymmetry. Doppler shift depends on the emitting plasma velocity. In Minkowski space, a rotating, optically thin ring will always appear brighter on the approaching side due to Doppler boosting: since the intensity I_ν on a line of sight and the frequency ν are invariant in the combination I_ν/ν^3, and ν is higher on the blueshifted side, then I_ν must be proportionately higher on the blueshifted side. This argument incorrectly suggests, however, that the brightness peak should always lie on the approaching side of the disk.

In the Kerr metric, a majority of the emission seen by EHT arises in a narrow ring close to the black hole at $r \sim 2$–$5\,GMc^{-2}$ (EHTC M87 V; G. N. Wong et al. 2022). There, Doppler shift interacts with other effects such as lensing. For a rapidly spinning hole with equatorial emission seen at small inclination, lines of sight (geodesics) that intersect the emission region tend to bend and wrap around the

Table 2
Gaussian Fits to Asymmetry

Spin	−0.97	−0.9375	−0.85	−0.75	−0.5	−0.25	0.0	0.25	0.5	0.75	0.85	0.9375	0.97
μ	0.653	0.609	0.567	0.485	0.382	0.324	0.278	0.378	0.525	0.573	0.630	0.645	0.675
σ	0.203	0.178	0.193	0.210	0.188	0.168	0.181	0.172	0.201	0.209	0.213	0.220	0.198

Note. Mode (μ) and standard deviation (σ) for truncated Gaussian fits to asymmetry distributions for MAD models. The fits are bounded by $a_1 \in [0, 1)$; we exclude $a_1 = 1$ cases prior to fitting.

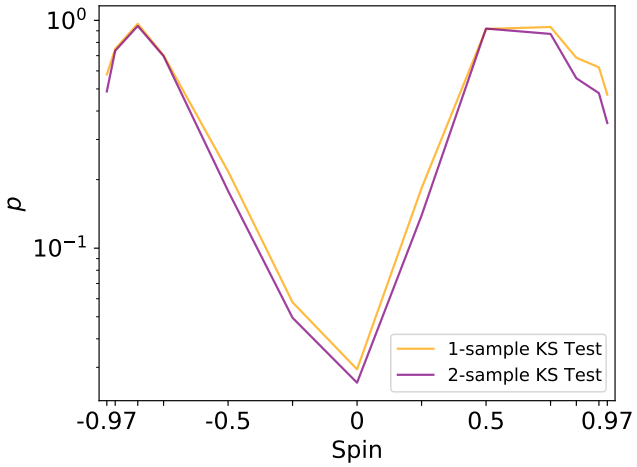

Figure 6. Probability p that the ensemble of MAD models at fixed spin is consistent with EHT data. The purple curve shows the results from the two-sample KS test against the full asymmetry distributions obtained for each spin. The yellow curve shows one-sample KS tests, with underlying asymmetry distributions replaced with best-fit truncated normal distributions. Parameters of these distributions are given in Table 2. The results are largely consistent.

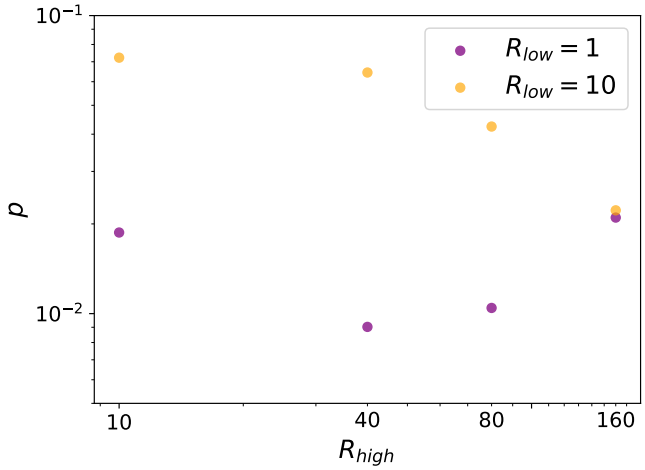

Figure 7. Probability p for zero-spin models, across $R_{\rm low} = 1$ (purple) and $R_{\rm low} = 10$ (yellow), based on two-sample KS tests. Models with $R_{\rm low} = 10$ are marginally favored.

hole in the spinward direction (M. D. Johnson et al. 2020). Thus for retrograde ($a_* < 0$) disks, direct lines of sight to the emission region emerge opposite the direction of rotation and are Doppler deboosted. Lensed, indirect lines of sight to the disk contribute comparatively more of the flux than in prograde disks.

The strength of Doppler boosting depends on plasma angular velocity. The angular velocity in the emission region is different in MAD (strongly magnetized) and SANE (weakly magnetized) models. This is evident in Figure 9 of V. Dhruv et al. (2025), which shows time- and azimuth-averaged angular momentum in the emission region for both MAD and SANE models. In MAD models, the plasma experiences strong magnetic torques in the plunging region, leading to slower rotation and thus weaker Doppler boosting. Since MAD models have relatively weak Doppler boosting, the asymmetry can be more sensitive to other effects.

The rotational velocity also differs between v3 and v5 models. This point is discussed in greater detail in Appendix A.

5.1. Comparison with Earlier Work

EHT reported asymmetries for both the 2017 and 2018 M87* datasets (EHTC M87 IV; EHTC M87 2018 I) that differ from those reported here. Those reports were based on either different parameterized image models, different definitions of asymmetry, or both.

The analysis of 2017 data reported an asymmetry $A \sim 0.22$ on April 11, which is smaller than reported here ($a_1 = 0.41$) due to a difference in definition. In that analysis, $A \equiv \left\langle \left| \int_0^{2\pi} I e^{i\theta} d\theta \right| / \int_0^{2\pi} I d\theta \right\rangle_{r \in [r_{\rm in}, r_{\rm out}]}$ on an annulus bounded by $r_{\rm in}$ and $r_{\rm out}$. If we apply this definition for A to an m-ring, the asymmetry recovered is a factor of 2 smaller than a_1, which is the amplitude of the $m = 1$ sinusoidal mode (see Equation (22) and subsequent discussion in EHTC M87 IV). The difference in definition accounts for most of the difference between their measurement and ours. The remainder is accounted for by a difference in measurement procedure: we fit a parameterized model, while the original EHT analysis did not.

The EHT analysis of 2018 April 21 data used Comrade and VIDA to measure an asymmetry and found $A \approx 0.31$ (other methods had the asymmetry ranging from $A \approx 0.21$ to 0.43, with an average of $A \approx 0.31$, per Table 7 of EHTC M87 2018 I). However, that analysis followed a Comrade convention where m-rings fitted in the (u, v) domain produce amplitudes that are a factor of $2\times$ smaller than those fitted in the image domain. Thus, their values typically range from $a_{1,\,UV} \in [0, 0.5]$. In our convention, we present both (u, v) and image domain asymmetries in units of $[\bar{I}_{\rm ring}]$ ranging from $a_1 \in [0, 1]$, where $a_1 = 1$ corresponds to a ring whose amplitude is as large as its mean intensity $\bar{I}_{\rm ring}$.

A smaller difference in asymmetry magnitude originates from the use of an mF-ring or floored m-ring model in the EHT 2018 analysis. This model has a flat (non-Gaussian) background, an elliptical ring, up to $m = 2$ modes (rather than $m = 4$), and allows for two free nuisance Gaussians to help

model diffuse extended emission. The nuisance Gaussians are allowed to overlap with the ring, and so can introduce on-ring brightness asymmetries that are not accounted for in their measure of asymmetry A. The more complex template from 2018 analysis allows for better fits to the 2018 data, while ours allows for more straightforward interpretation at reduced computational cost.

The EHT analysis of 2021 April 18 used Comrade to measure an asymmetry of $A \approx 0.22-0.25$, again following the convention where values of A are a factor of 2 smaller than a_1. Their analysis used an $m = 4$ m-ring as in this work, but had minor differences in the background Gaussian component (see Section 3.4 and Table 2 in EHTC M87 2021). Their recovered values of A are consistent with a_1 measured in this work, after accounting for these differences.

The theoretical study of ring asymmetry in EHT images has focused mainly on inclination, rather than spin. L. Medeiros et al. (2022) analyzed asymmetry in M87* with a focus on the inclination dependence, using a set of GRMHD models. Their measure of asymmetry is based on integrations along rays through the image at fixed position angle, comparing the line-integrated intensity on one side of the shadow against the other. Assuming that $a_3 \ll a_1$ (as in most of our fits), their asymmetry measure $A \approx (1 + a_1)/(1 - a_1)$. They consider GRMHD models with $a_* = 0, 0.7, 0.9$ and see relatively little asymmetry at zero spin. L. Medeiros et al. (2022) find a strong dependence on inclination, and also note a substantial difference between MAD and SANE models.

R. Qiu et al. (2023) have used machine learning models trained on a different set of GRMHD simulations to assess relative importance of different image observables for spin and inclination inference. Asymmetry, computed as in L. Medeiros et al. (2022), was included as one of the observables. They find that asymmetry has moderate to strong effects on spin and inclination constraints, broadly consistent with our results. The authors find that observation of asymmetry puts particularly strong constraints on spin for Sgr A* models. For M87* models, the constraining power of asymmetry is smaller, but is still the highest among all observables not pertaining to polarization structure. In our study, the v5 simulations sample black hole spin more densely and use what we believe to be a more accurate adiabatic index (C. F. Gammie 2025).

J. C. Faggert et al. (2025) studied asymmetry in a phenomenological thick-disk model. They use yet another measure of asymmetry, FA, which relies on the depth of nulls in the visibility amplitudes on rays perpendicular to the projection of the spin axis on the sky. In the limit of a thin ring (not always appropriate), one can show that $FA \approx a_1 J_1(j_{0,1}) \approx 0.52 a_1$, where $j_{0,1}$ is the first root of $J_0(x)$, while $J_0(x)$ and $J_1(x)$ are zeroth and first Bessel functions of the first kind. They also introduce a second metric, $IA \equiv A - 1$, where A is the L. Medeiros et al. (2022) asymmetry. For 2017 M87* data they find $FA = 0.20$–0.24, implying $a_1 \approx 0.38$–0.46, consistent with the $a_1 = 0.41$ value we find by fitting all visibility amplitudes and closure phases using Comrade. J. C. Faggert et al. (2025) find that FA depends strongly on inclination and is almost independent of spin at inclinations appropriate to M87* (see their Figure 4), which differs significantly from our results. This is likely due to differences in the underlying disk model.

Saurabh et al. (2026) perform a detailed study of asymmetry dependence on geometric parameters, including spin, in semianalytic RIAF models, as well as in a subset of GRMHD simulations. They define asymmetry as the ratio of total imaged fluxes on both sides of the black hole's rotation axis. The authors find that RIAF models tend to produce more symmetric images than GRMHD ones, possibly due to the simplifying assumptions on the magnetic field structure and fluid flow in RIAF models. Despite that, both RIAF and GRMHD models demonstrate asymmetry growth with $|a_*|$ and disfavor small negative a_* models as too symmetric, which broadly agrees with our findings.

5.2. Future EHT Observations

Future upgrades to EHT and future observations will improve our understanding of the ring asymmetry in M87* and Sgr A*. In both sources, the emitting plasma is turbulent and samples a turbulent configuration about once per correlation time $\tau_{\rm corr}$. For the asymmetry magnitude, the correlation time $\tau_{\rm corr}(a_1) \approx 95\, t_g$ across the full model library. For MAD models, $\tau_{\rm corr}(a_1) \approx 115\, t_g$. Thus for M87*, $\tau_{\rm corr} \approx 100\, t_g \approx 35$ days and for Sgr A* $\tau_{\rm corr} \approx 30$ minutes.

In Sgr A*, which we have not discussed yet, instantaneous (u, v) coverage is poor compared with M87*. Each turbulent configuration persists for only $\sim$30 minutes, during which Earth's rotation causes the baselines to trace out only short arcs in the (u, v) plane. Thus, Sgr A*'s asymmetry is comparatively poorly constrained. The addition of new antennas can improve coverage, allow better asymmetry estimates, and enable a model-dependent constraint on the inclination and spin of Sgr A*.

In M87*, each turbulent configuration persists for $\sim$35 days; during a night of observation, the source changes very little, but Earth's rotation causes the baselines to trace out long arcs in the (u, v) plane (so-called Earth rotation aperture synthesis). As shown in Figure 3, this coverage permits accurate asymmetry measurements. At present, there are three snapshots from uncorrelated turbulent configurations separated by a year, in 2017, 2018, and 2021. The uncertainty in the measurement of the average asymmetry scales with the number of independent samples N as $\sim\sigma/\sqrt{N}$, where σ is the width of the "true" asymmetry distribution ($\sigma \simeq 0.2$, per Table 2). Existing data that has not been analyzed yet, from 2022 to 2024, will take N from 3 to 6. We forecast that this will reduce uncertainty in the mean asymmetry by $\sim 1/\sqrt{2}$.

ALMA has recently approved a time-lapse imaging campaign of M87* in 2026. If the asymmetry correlation times in M87* and models are consistent, then the main campaign will span $\sim$2 correlation times, while potential extensions would enable up to $\sim$4 independent measurements. Taken with 2025 observations and potential future observations in 2027+, EHT could achieve 12 independent samples by the end of the decade, reducing uncertainty in the mean asymmetry by a factor of $\sim 1/2$.

To assess how future observations might constrain spin, we consider two scenarios: one showing the confidence with which spin zero models can be ruled out assuming future observations that are consistent with present constraints, and another showing how well the spin can be measured if the true asymmetry distribution in M87* is well described by one of our models.

For the first case, we assume the asymmetry is a (truncated) normal distribution with μ equal to the average of the three existing measurements, $\sim$0.55, and the standard deviation

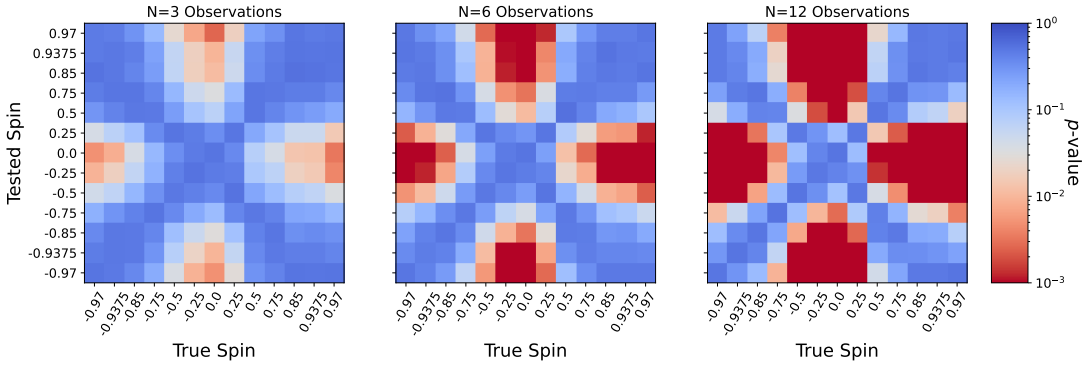

Figure 8. Effect of new observations on spin constraints. We repeatedly "observe" N random asymmetry samples from the MAD model distribution for each "true" spin, then compare the mock observations to the asymmetry distribution for each "tested" spin using a KS test. The resulting median probability p of each tested spin is shown for $N = 3$ observations (left), $N = 6$ (center), and $N = 12$ (right). High p (blue) suggests the asymmetry distribution in the tested spin is a good match to the observations of the true spin; low p (red) suggests we can rule out the tested spin. As N increases, we can correctly rule out an increasing fraction of the parameter space.

$\simeq$0.2, motivated by the typical standard deviation in the model library. We draw N random samples (mock observations) from the truncated normal distribution, and perform a KS test comparing the mock observations to all spin zero models. For each N, we repeat this procedure many times. We find the median p for spin zero drops off as $p \sim e^{-N/1.6}$: the constraint improves exponentially as new observations are added.

For the second case, we assume the correct model is in our library and ask how well future observations can measure the spin. The result is shown in Figure 8. We fix the "true" spin of M87*, draw samples from the distribution for that spin reported in Table 2, and test the N simulated observations against the model distribution at each spin. We again repeat this procedure many times and take the median p. The resulting p for different M87* spins and observational samples N are shown in Figure 8. The p-value recovered for the true spin lies on the "True Spin = Tested Spin" diagonal. If M87* is highly spinning, we will be able to strongly exclude zero-spin models by $N = 6$. If on the other hand M87* has low spin, we will also be able to strongly exclude high spin by $N = 6$.

5.3. Degeneracy with Inclination

So far, we have only considered $i = 17°$ and 163°. As earlier works such as L. Medeiros et al. (2022) have noted, however, the asymmetry also varies with inclination. When face-on at $i = 0°$ or 180°, we would expect $a_1 = 0$; when edge-on, we would expect a_1 to reach its maximum. To what degree does the uncertainty in M87*'s estimated inclination (with standard deviation $\approx$3°–4°, per F. Mertens et al. 2016; R. C. Walker et al. 2018) contaminate our spin constraints?

We assess the uncertainty introduced by inclination error in a small sample of models, changing the inclination by $\pm 5°$ from the inclination used in our standard model series. We consider four MAD models, with $R_{\rm high} = 40$, $R_{\rm low} = 1$, and $a_* = \pm 0.5$. We sample 30 images from each model separated by $>50\,t_g$. In the prograde model, we find a shift of $i \pm 5°$ corresponds to a shift in asymmetry of $a_1 \pm 0.1$. In the retrograde model, we find a shift of $i \pm 5°$ corresponds to a shift in asymmetry of $a_1 \pm 0.04$. The asymmetry uncertainty due to inclination error σ_i will begin to dominate when $\sigma/\sqrt{N} < \sigma_i$ for N independent samples and asymmetry distribution standard deviation σ. This occurs when $N \gtrsim 4$ for the retrograde models, and $N \gtrsim 25$ for the prograde models.

5.4. Model Uncertainty

Our asymmetry distributions are model-dependent. What are the sources of model uncertainty?

Two uncertainties (magnetization and adiabatic index) are discussed in detail in Appendix A, since they can be evaluated from existing simulation data. To summarize: across v3 and v5 MAD and SANE models, the asymmetry is minimized at zero or at slightly negative spin, although the exact relationship between asymmetry and spin shows some variation. Additional sources of model uncertainty include the following:

(1) Electron energization and thermodynamics. Our models assume the electron distribution function is thermal with $T_e(\beta, T_i; R_{\rm high}, R_{\rm low})$, $T_e \ll T_i$, and with an isotropic T_e relative to the local magnetic field. Better models would evolve a separate electron internal energy equation. This may produce better agreement of the models with Sgr A* variability data (L. Salas et al. 2025), although it requires modeling electron heating (an unsettled issue in the theory of collisionless plasmas), electron cooling (particularly important in M87*), and acceleration of electrons into a nonthermal tail.

GRMHD models with the nonthermal tail in the electron distribution function produce remarkably similar brightness asymmetries to their thermal counterparts (see EHTC M87 2018 II, Figure 3). One set of GRMHD models that evolve a separate electron internal energy shows similar trends in asymmetry, but has a decrease in the overall magnitude by $\sim$33% after accounting for a different asymmetry definition, which should produce values 2$\times$ smaller than ours if the data corresponds to an $m = 1$ m-ring (A. Chael 2025). If the decrease is due to the differing models and not the differing asymmetry definition, then the smaller asymmetry would allow us to more confidently rule out zero spin.

Electron anisotropy can also affect asymmetry (A. Galishnikova et al. 2023). Anisotropy perpendicular to the magnetic field ($T_\perp > T_\parallel$, as in the mirror and whistler limits) produces increased asymmetry in the image and is disfavored based on the observed circular polarization fraction (V. L. Ginzburg & S. I. Syrovatskii 1965; A. Galishnikova et al. 2023; EHTC M87 IX). Anisotropy parallel to the magnetic field ($T_\parallel > T_\perp$, as in the firehose limit)

would decrease the observed asymmetry, thus increasing the confidence with which we could rule out zero spin.

(2) Collisionless dynamics. Our models treat the accreting plasma as an ideal fluid, but the plasma is known to be Coulomb-collisionless.[172] The accuracy of this approximation is not yet understood. Although Coulomb scattering is too weak to fluidize the plasma, wave–particle scattering may be strong enough (e.g., M. W. Kunz et al. 2014). One particular source of concern is that, at least for some model problems, the reconnection rate is an order of magnitude slower in MHD than in kinetic theory (e.g., B. Ripperda et al. 2020). Models that incorporate nonideal corrections (viscosity and heat conduction) to an ideal fluid show behavior that is remarkably similar to ideal models (F. Foucart et al. 2017; V. Dhruv et al. 2025).

(3) Boundary and initial conditions. The models are initialized with a magnetized torus of limited radial extent (L. G. Fishbone & V. Moncrief 1976; G. N. Wong et al. 2022). The variation of model outcomes with respect to changes in this initial condition and boundary conditions have not yet been fully assessed. It is known that in models of Sgr A*, a limited set of self-consistent wind-fed models (S. M. Ressler et al. 2020) produce images that are similar to images produced with our initial conditions used here (EHTC SgrA V).

(4) The "fast light" approximation. The fast light approximation used here performs the radiative transfer calculation for a snapshot on a single time slice. A more precise treatment ("slow light") would trace the photon trajectories through multiple time slices, i.e., through the fluid as it evolves, since the light-crossing time is only slightly less than the dynamical time close to the horizon. The fast light approximation is used because it is cheap and simple. We have compared the asymmetry distribution in fast light and slow light versions of a test model and find that they are nearly identical. The asymmetry had a mean and standard deviation of 0.70 ± 0.18 in the fast light model, while it was 0.70 ± 0.19 in the slow light model.

Finally, there are other sources of uncertainty such as those related to numerical treatment of low-density regions in the flow. Ultimately the models will be tested by comparison with observations.

5.5. Testing the Blandford–Znajek Jet-launching Mechanism

The Blandford–Znajek (BZ) mechanism (R. D. Blandford & R. L. Znajek 1977) is commonly considered the favored mechanism for jet launching. BZ predicts (1) that there is a black hole at the base of M87*'s jet, (2) that the jet connects to the black hole, (3) that the black hole is spinning, and (4) that the jet power is a function of black hole spin. The presence of a black hole is unambiguously confirmed by 230 GHz VLBI imaging, which shows the expected ring (EHTC M87 I). 86 GHz VLBI imaging shows a connection between the black hole and jet (R.-S. Lu et al. 2023). Our analysis suggests that the black hole is spinning—consistent with BZ. Estimates of M87*'s jet power typically favor higher spins assuming BZ (R. Nemmen 2019; EHTC M87 V), and these higher spins are among the values favored by asymmetry. In Section 5.2, we show future observations may provide improved spin constraints. Future EHT or space-VLBI observations could test BZ by checking for continued consistency between estimates of spin and jet power. Finally, future observations may also provide a direct probe of the electromagnetic energy extraction direction using polarization measurements, which could also test BZ (A. Chael et al. 2023).

[172] Ideal here refers to the governing equations. The numerical implementation, which is an ILES or Implicit Large Eddy Simulation, still incorporates dissipation due to truncation error at the grid scale. See P. Grete et al. (2023) for a discussion of ILES in compressible MHD.

6. Conclusion

In this paper, we have presented tentative evidence for a spinning M87* black hole based on the asymmetry of 2017, 2018, and 2021 EHT images. The evidence is tentative because it relies on (1) the relevance of the model library itself, which is known to have missing physical ingredients and internal inconsistencies, discussed in Section 5.4; (2) a restriction of the model library to magnetically arrested disk (MAD) models, which are nevertheless preferred by EHT data; and (3) only three independent observations. With these assumptions, zero-spin models are disfavored.

The spin-ring asymmetry correlation is clearer for MAD models than for SANE models (see Appendix A), and MAD models are mildly favored by existing model–data comparisons. SANEs are more likely to fail the jet power constraint (EHTC M87 V). SANEs are also either too weakly polarized, or have weak magnetic field lines that become too azimuthal as they are dragged by the fluid, producing EVPAs that are too radial to agree with the observed orientations (EHTC M87 VIII).

At present, there are three independent asymmetry measurements for M87*. This paper highlights the value of new data for constraining the spin of M87*. In Section 5.2, we have calculated the median probability that the observations are drawn from an $a_* = 0$ model asymmetry distribution to scale as $\exp(-N/1.6)$, where N is the number of independent asymmetry measurements.

Our analysis, based on image asymmetry alone, suggests that M87* may have $|a_*| \gtrsim 0.2$, as can be seen in Figure 6. In particular, $a_* = 0$ and -0.25 models are marginally disfavored at $p \approx 0.026$ and 0.049, respectively. Models with $a_* = 0.25$ are currently still plausible at $p \approx 0.14$. The EHT could strengthen its spin constraints with an increased sample size, e.g., using future time-lapse imaging of M87*. This is consistent with previous arguments based on jet power (EHTC M87 V): low-spin models that match the compact millimeter flux of M87*'s accretion disk have jet power far below existing estimates. Our argument here is independent of the jet power argument and does not rely on highly uncertain jet power estimates.

Our spin constraint is also consistent with spin distributions obtained in M. Janssen et al. (2025), which uses machine learning models trained on GRMHD simulations to interpret polarized data. Our analysis does not use M87* polarization data. The EHT could also strengthen its spin constraints by incorporating other observables, such as the aforementioned jet power, polarization structure of the ring (D. C. M. Palumbo et al. 2020; A. Chael et al. 2023), and pattern speed (N. S. Conroy et al. 2023).

The asymmetry argument presented here, the jet power argument (EHTC M87 V), and the outcome of GRMHD simulations (e.g., J. C. McKinney & C. F. Gammie 2004) are all consistent with the notion that the M87* jet is powered by

the BZ mechanism. We outline several methods to test predictions of the BZ mechanism with future observations.

A future space-based VLBI antenna, such as the proposed NASA BHEX mission (M. D. Johnson et al. 2024), would enable us to resolve near-horizon rings in sources other than M87* and Sgr A* (X. A. Zhang et al. 2024). Our work suggests that it may be possible to estimate the magnitude of spin in these sources based on asymmetry alone, if a sufficiently good estimate for the inclination is available. Ring diameter and brightness asymmetry are perhaps the easiest features to measure in EHT images, thus enabling future analysis to provide model-dependent constraints on mass and spin across a variety of sources.

Acknowledgments

We thank the anonymous referee for their thorough comments, which greatly improved this work. This work was supported by NSF grants AST 17-16327 (horizon), OISE 17-43747, and AST 20-34306. This material is based upon work supported by the National Science Foundation under grant No. PHY-2244433. N.C. is supported by the NASA Future Investigators in NASA Earth and Space Science and Technology (FINESST) program. This material is based upon work supported by the National Aeronautics and Space Administration under grant No. 80NSSC24K1475 issued through the Science Mission Directorate. This research used resources of the Oak Ridge Leadership Computing Facility at the Oak Ridge National Laboratory, which is supported by the Office of Science of the U.S. Department of Energy under Contract No. DE-AC05-00OR22725. This research used resources of the Argonne Leadership Computing Facility, which is a DOE Office of Science User Facility supported under Contract DE-AC02-06CH11357. This research was done using services provided by the OSG Consortium, which is supported by the National Science Foundation awards #2030508 and #1836650. This research is part of the Delta research computing project, which is supported by the National Science Foundation (award OCI 2005572), and the State of Illinois. Delta is a joint effort of the University of Illinois at Urbana-Champaign and its National Center for Supercomputing Applications. We are particularly grateful to the Argonne Leadership Computing Facility for providing storage space on the Eagle system that was critical for enabling this work. This work was initiated in part at the Aspen Center for Physics, which is supported by National Science Foundation grant PHY-2210452.

The Event Horizon Telescope Collaboration thanks the following organizations and programs: the Academia Sinica; the Research Council of Finland (project 362572); the Agencia Nacional de Investigación y Desarrollo (ANID), Chile via NCN19_058 (TITANs), Fondecyt 1221421 and BASAL FB210003; the Alexander von Humboldt Stiftung (including the Feodor Lynen Fellowship); an Alfred P. Sloan Research Fellowship; Allegro, the European ALMA Regional Centre node in the Netherlands, the NL astronomy research network NOVA and the astronomy institutes of the University of Amsterdam, Leiden University, and Radboud University; the ALMA North America Development Fund; the Astrophysics and High Energy Physics programme by MCIN (with funding from European Union NextGenerationEU, PRTR-C17I1); the black hole Initiative, which is funded by grants from the John Templeton Foundation (60477, 61497, 62286) and the Gordon and Betty Moore Foundation (grant GBMF-8273)—although the opinions expressed in this work are those of the author and do not necessarily reflect the views of these Foundations; the Brinson Foundation; the Canada Research Chairs (CRC) program; Chandra DD7-18089X and TM6-17006X; the China Scholarship Council; the China Postdoctoral Science Foundation fellowships (2020M671266, 2022M712084); ANID through Fondecyt Postdoctorado (project 3250762); Conicyt through Fondecyt Postdoctorado (project 3220195); Consejo Nacional de Humanidades, Ciencia y Tecnología (CONAHCYT, Mexico, projects U0004-246083, U0004-259839, F0003-272050, M0037-279006, F0003-281692, 104497, 275201, 263356, CBF2023-2024-1102, 257435); the Colfuturo Scholarship; the Consejo Superior de Investigaciones Científicas (grant 2019AEP112); the Delaney Family via the Delaney Family John A. Wheeler Chair at Perimeter Institute; Dirección General de Asuntos del Personal Académico-Universidad Nacional Autónoma de México (DGAPA-UNAM, projects IN112820 and IN108324); the Dutch Research Council (NWO) for the VICI award (grant 639.043.513), the grant OCENW.KLEIN.113, and the Dutch black hole Consortium (with project No. NWA 1292.19.202) of the research programme the National Science Agenda; the Dutch National Supercomputers, Cartesius and Snellius (NWO grant 2021.013); the EACOA Fellowship awarded by the East Asia Core Observatories Association, which consists of the Academia Sinica Institute of Astronomy and Astrophysics, the National Astronomical Observatory of Japan, Center for Astronomical Mega-Science, Chinese Academy of Sciences, and the Korea Astronomy and Space Science Institute; the European Research Council (ERC) Synergy Grant "BlackHoleCam: Imaging the Event Horizon of Black Holes" (grant 610058) and Synergy Grant "BlackHolistic: Colour Movies of Black Holes: Understanding black hole Astrophysics from the Event Horizon to Galactic Scales" (grant 10107164); the European Union Horizon 2020 research and innovation programme under grant agreements RadioNet (No. 730562), M2FINDERS (No. 101018682); the European Research Council for advanced grant "JETSET: Launching, propagation and emission of relativistic jets from binary mergers and across mass scales" (grant No. 884631); the European Horizon Europe staff exchange (SE) programme HORIZON-MSCA-2021-SE-01 grant NewFunFiCO (No. 10108625); the Horizon ERC grants 2021 programme under grant agreement No. 101040021; the FAPESP (Fundação de Amparo á Pesquisa do Estado de São Paulo) under grant 2021/01183-8; the Fondes de Recherche Nature et Technologies (FRQNT); the Fondo CAS-ANID folio CAS220010; the Generalitat Valenciana (grants APOSTD/2018/177 and ASFAE/2022/018) and GenT Program (project CIDEGENT/2018/021); the Gordon and Betty Moore Foundation (GBMF-3561, GBMF-5278, GBMF-10423); the Institute for Advanced Study; the ICSC—Centro Nazionale di Ricerca in High Performance Computing, Big Data and Quantum Computing, funded by European Union—NextGenerationEU; the Istituto Nazionale di Fisica Nucleare (INFN) sezione di Napoli, iniziative specifiche TEONGRAV; the International Max Planck Research School for Astronomy and Astrophysics at the Universities of Bonn and Cologne; the Italian Ministry of University and Research (MUR)—Project CUP F53D23001260001, funded by the European Union—NextGenerationEU; Deutsche Forschungsgemeinschaft (DFG) research grant "Jet physics on horizon

scales and beyond" (grant No. 443220636) and DFG research grant 443220636; Joint Columbia/Flatiron Postdoctoral Fellowship (research at the Flatiron Institute is supported by the Simons Foundation); the Japan Ministry of Education, Culture, Sports, Science and Technology (MEXT; grant JPMXP1020200109); the Japan Society for the Promotion of Science (JSPS) Grant-in-Aid for JSPS Research Fellowship (JP17J08829); the Joint Institute for Computational Fundamental Science, Japan; the Key Research Program of Frontier Sciences, Chinese Academy of Sciences (CAS, grants QYZDJSSW-SLH057, QYZDJSSW-SYS008, ZDBS-LY-SLH011); the Leverhulme Trust Early Career Research Fellowship; the Max-Planck-Gesellschaft (MPG); the Max Planck Partner Group of the MPG and the CAS; the MEXT/JSPS KAKENHI (grants 18KK0090, JP21H01137, JP18H03721, JP18K13594, 18K03709, JP19K14761, 18H01245, 25120007, 19H01943, 21H01137, 21H04488, 22H00157, 23K03453); the MICINN Research Projects PID2019-108995GB-C22, PID2022-140888NB-C22; the MIT International Science and Technology Initiatives (MISTI) Funds; the Ministry of Science and Technology (MOST) of Taiwan (103-2119-M-001-010-MY2, 105-2112-M-001-025-MY3, 105-2119-M-001-042, 106-2112-M-001-011, 106-2119-M-001-013, 106-2119-M-001-027, 106-2923-M-001-005, 107-2119-M-001-017, 107-2119-M-001-020, 107-2119-M-001-041, 107-2119-M-110-005, 107-2923-M-001-009, 108-2112-M-001-048, 108-2112-M-001-051, 108-2923-M-001-002, 109-2112-M-001-025, 109-2124-M-001-005, 109-2923-M-001-001, 110-2112-M-001-033, 110-2124-M-001-007, and 110-2923-M-001-001); the National Science and Technology Council (NSTC) of Taiwan (111-2124-M-001-005, 112-2124-M-001-014, 112-2112-M-003-010-MY3, and 113-2124-M-001-008); the Ministry of Education (MoE) of Taiwan Yushan Young Scholar Program; the Physics Division, National Center for Theoretical Sciences of Taiwan; the National Aeronautics and Space Administration (NASA, Fermi Guest Investigator grant 80NSSC23K1508, NASA Astrophysics Theory Program grant 80NSSC20K0527, NASA NuSTAR award 80NSSC20K0645); NASA Hubble Fellowship Program Einstein Fellowship; NASA Hubble Fellowship grants HST-HF2-51431.001-A, HST-HF2-51482.001-A, HST-HF2-51539.001-A, HST-HF2-51552.001A awarded by the Space Telescope Science Institute, which is operated by the Association of Universities for Research in Astronomy, Inc., for NASA, under contract NAS5-26555; the National Institute of Natural Sciences (NINS) of Japan; the National Key Research and Development Program of China (grant 2016YFA0400704, 2017YFA0402703, 2016YFA0400702); the National Science and Technology Council (NSTC, grants NSTC 111-2112-M-001 -041, NSTC 111-2124-M-001-005, NSTC 112-2124-M-001-014); the US National Science Foundation (NSF, grants AST-0096454, AST-0352953, AST-0521233, AST-0705062, AST-0905844, AST-0922984, AST-1126433, OIA-1126433, AST-1140030, DGE-1144085, AST-1207704, AST-1207730, AST-1207752, MRI-1228509, OPP-1248097, AST-1310896, AST-1440254, AST-1555365, AST-1614868, AST-1615796, AST-1715061, AST-1716327, AST-1726637, OISE-1743747, AST-1743747, AST-1816420, AST-1935980, AST-1952099, AST-20-34306, AST-2205908, AST-2307887, AST-2407810); NSF Astronomy and Astrophysics Postdoctoral Fellowship (AST-1903847); the Natural Science Foundation of China (grants 11650110427, 10625314, 11721303, 11725312, 11873028, 11933007, 11991052, 11991053, 12192220, 12192223, 12273022, 12325302, 12303021); the Natural Sciences and Engineering Research Council of Canada (NSERC); the National Research Foundation of Korea (the Global PhD Fellowship Grant: grants NRF-2015H1A2A1033752; the Korea Research Fellowship Program: NRF-2015H1D3A1066561; Brain Pool Program: RS-2024-00407499; Basic Research Support grant 2019R1F1A1059721, 2021R1A6A3A01086420, 2022R1C1C1005255, RS-2022-NR071771, 2022R1F1A1075115); the POSCO Science Fellowship of the POSCO TJ Park Foundation; NOIRLab, which is managed by the Association of Universities for Research in Astronomy (AURA) under a cooperative agreement with the National Science Foundation; Onsala Space Observatory (OSO) national infrastructure, for the provisioning of its facilities/observational support (OSO receives funding through the Swedish Research Council under grant 2017-00648); the Perimeter Institute for Theoretical Physics (research at Perimeter Institute is supported by the Government of Canada through the Department of Innovation, Science and Economic Development and by the Province of Ontario through the Ministry of Research, Innovation and Science); the Portuguese Foundation for Science and Technology (FCT) grants (Individual CEEC program—5th edition, CIDMA through the FCT Multi-Annual Financing Program for R&D Units UID/04106, CERN/FIS-PAR/0024/2021, 2022.04560.PTDC); the Princeton Gravity Initiative; the Spanish Ministerio de Ciencia, Innovación y Universidades (grants PID2022-140888NB-C21, PID2022-140888NB-C22, PID2023-147883NB-C21, RYC2023-042988-I); the Severo Ochoa grant CEX2021-001131-S funded by MICIU/AEI/10.13039/501100011033; The European Union's Horizon Europe research and innovation program under grant agreement No. 101093934 (RADIOBLOCKS); The European Union "NextGenerationEU," the Recovery, Transformation and Resilience Plan, the CUII of the Andalusian Regional Government and the Spanish CSIC through grant AST22_00001_Subproject_10; "la Caixa" Foundation (ID 100010434) through fellowship codes LCF/BQ/DI22/11940027 and LCF/BQ/DI22/11940030; the University of Pretoria for financial aid in the provision of the new Cluster Server nodes and SuperMicro (USA) for a SEEDING GRANT approved toward these nodes in 2020; the Shanghai Municipality orientation program of basic research for international scientists (grant no. 22JC1410600); the Shanghai Pilot Program for Basic Research, Chinese Academy of Science, Shanghai Branch (JCYJ-SHFY-2021-013); the Simons Foundation (grant 00001470); the Spanish Ministry for Science and Innovation grant CEX2021-001131-S funded by MCIN/AEI/10.13039/501100011033; the Spinoza Prize SPI 78-409; the South African Research Chairs Initiative, through the South African Radio Astronomy Observatory (SARAO, grant ID 77948), which is a facility of the National Research Foundation (NRF), an agency of the Department of Science and Innovation (DSI) of South Africa; the Swedish Research Council (VR); the Taplin Fellowship; the Toray Science Foundation; the UK Science and Technology Facilities Council (grant No. ST/X508329/1); the US Department of Energy (USDOE) through the Los Alamos National Laboratory (operated by Triad National Security, LLC, for the National Nuclear Security Administration of the USDOE, contract 89233218CNA000001); and the YCAA Prize Postdoctoral Fellowship. This work was also supported by the National Research Foundation of Korea (NRF) grant funded by the Korea government (MSIT) (RS-2024-00449206). We

acknowledge support from the Coordenação de Aperfeiçoamento de Pessoal de Nível Superior (CAPES) of Brazil through PROEX grant No. 88887.845378/2023-00. We acknowledge financial support from Millenium Nucleus NCN23_002 (TITANs) and Comité Mixto ESO-Chile.

We thank the staff at the participating observatories, correlation centers, and institutions for their enthusiastic support. This paper makes use of the following ALMA data: ADS/JAO.ALMA#2017.1.00841.V and ADS/JAO.ALMA#2019.1.01797.V. ALMA is a partnership of the European Southern Observatory (ESO; Europe, representing its member states), NSF, and National Institutes of Natural Sciences of Japan, together with National Research Council (Canada), Ministry of Science and Technology (MOST; Taiwan), Academia Sinica Institute of Astronomy and Astrophysics (ASIAA; Taiwan), and Korea Astronomy and Space Science Institute (KASI; Republic of Korea), in cooperation with the Republic of Chile. The Joint ALMA Observatory is operated by ESO, Associated Universities, Inc. (AUI)/NRAO, and the National Astronomical Observatory of Japan (NAOJ). The NRAO is a facility of the NSF operated under cooperative agreement by AUI. This research used resources of the Oak Ridge Leadership Computing Facility at the Oak Ridge National Laboratory, which is supported by the Office of Science of the U.S. Department of Energy under contract No. DE-AC05-00OR22725; the ASTROVIVES FEDER infrastructure, with project code IDIFEDER-2021-086; the computing cluster of Shanghai VLBI correlator supported by the Special Fund for Astronomy from the Ministry of Finance in China; We also thank the Center for Computational Astrophysics, National Astronomical Observatory of Japan. This work was supported by FAPESP (Fundacao de Amparo a Pesquisa do Estado de Sao Paulo) under grant 2021/01183-8.

APEX is a collaboration between the Max-Planck-Institut für Radioastronomie (Germany), ESO, and the Onsala Space Observatory (Sweden). The SMA is a joint project between the SAO and ASIAA and is funded by the Smithsonian Institution and the Academia Sinica. The JCMT is operated by the East Asian Observatory on behalf of the NAOJ, ASIAA, and KASI, as well as the Ministry of Finance of China, Chinese Academy of Sciences, and the National Key Research and Development Program (No. 2017YFA0402700) of China and Natural Science Foundation of China grant 11873028. Additional funding support for the JCMT is provided by the Science and Technologies Facility Council (UK) and participating universities in the UK and Canada. The LMT is a project operated by the Instituto Nacional de Astrófisica, Óptica, y Electrónica (Mexico) and the University of Massachusetts at Amherst (USA). The IRAM 30 m telescope on Pico Veleta, Spain, and the NOEMA interferometer on Plateau de Bure, France, are operated by IRAM and supported by CNRS (Centre National de la Recherche Scientifique, France), MPG (Max-Planck-Gesellschaft, Germany), and IGN (Instituto Geográfico Nacional, Spain). The SMT is operated by the Arizona Radio Observatory, a part of the Steward Observatory of the University of Arizona, with financial support of operations from the State of Arizona and financial support for instrumentation development from the NSF. Support for SPT participation in the EHT is provided by the National Science Foundation through award OPP-1852617 to the University of Chicago. Partial support is also provided by the Kavli Institute of Cosmological Physics at the University of Chicago. The SPT hydrogen maser was provided on loan from the GLT, courtesy of ASIAA.

This work used the Extreme Science and Engineering Discovery Environment (XSEDE), supported by NSF grant ACI-1548562, and CyVerse, supported by NSF grants DBI-0735191, DBI-1265383, and DBI-1743442. XSEDE Stampede2 resource at TACC was allocated through TG-AST170024 and TG-AST080026N. XSEDE JetStream resource at PTI and TACC was allocated through AST170028. This research is part of the Frontera computing project at the Texas Advanced Computing Center through the Frontera Large-Scale Community Partnerships allocation AST20023. Frontera is made possible by National Science Foundation award OAC-1818253. This research was done using services provided by the OSG Consortium (R. Pordes et al. 2007; A. Roy & OSG Consortium 2009), which is supported by the National Science Foundation award Nos. 2030508 and 1836650. Additional work used ABACUS2.0, which is part of the eScience center at Southern Denmark University, and the Kultrun Astronomy Hybrid Cluster (projects Conicyt Programa de Astronomia Fondo Quimal QUIMAL170001, Conicyt PIA ACT172033, Fondecyt Iniciacion 11170268, Quimal 220002). Simulations were also performed on the SuperMUC cluster at the LRZ in Garching, on the LOEWE cluster in CSC in Frankfurt, on the HazelHen cluster at the HLRS in Stuttgart, and on the Pi2.0 and Siyuan Mark-I at Shanghai Jiao Tong University. The computer resources of the Finnish IT Center for Science (CSC) and the Finnish Computing Competence Infrastructure (FCCI) project are acknowledged. This research was enabled in part by support provided by Compute Ontario (http://computeontario.ca), Calcul Quebec (http://www.calculquebec.ca), and the Digital Research Alliance of Canada (https://alliancecan.ca/en).

The EHTC has received generous donations of FPGA chips from Xilinx Inc., under the Xilinx University Program. The EHTC has benefited from technology shared under open-source license by the Collaboration for Astronomy Signal Processing and Electronics Research (CASPER). The EHT project is grateful to T4Science and Microsemi for their assistance with hydrogen masers. This research has made use of NASA's Astrophysics Data System. We gratefully acknowledge the support provided by the extended staff of the ALMA, from the inception of the ALMA Phasing Project through the observational campaigns of 2017 and 2018. We would like to thank A. Deller and W. Brisken for EHT-specific support with the use of DiFX. We thank Martin Shepherd for the addition of extra features in the Difmap software that were used for the CLEAN imaging results presented in this paper. We acknowledge the significance that Maunakea, where the SMA and JCMT EHT stations are located, has for the indigenous Hawaiian people.

Appendix A
Other Model Sets

A.1. v3 Illinois GRMHD Library

In this study, we rely on the v5 version of the PATOKA model library. This version has significant differences from version v3. The most notable physical difference is that in v5, the plasma adiabatic index is $\gamma = \frac{5}{3}$, compared with $\gamma = \frac{4}{3}$ in v3. Models in v5 were run longer, at higher resolution, with a

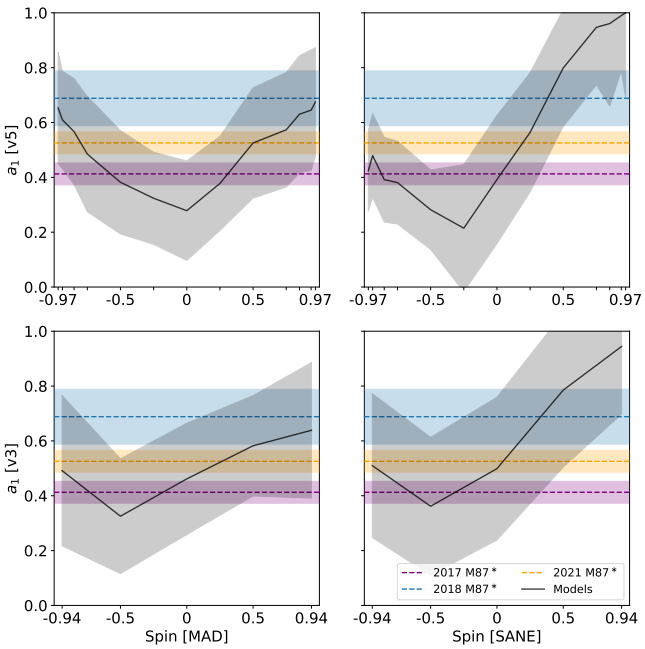

Figure 9. Asymmetry curves with 1σ ranges, as in Figure 5, for v5 MAD (top left), v5 SANE (top right), v3 MAD (bottom left), and v3 SANE (bottom right) models. The black lines show the modes μ of truncated Gaussians fitted to modeled asymmetry distributions at each spin. The gray bands show the 1σ variation of the distributions. Observed asymmetries in M87* are marked with dashed lines. The colored bands show 1σ uncertainties. *X*-axis tick marks show the spins sampled in each set of models.

slight change in $R_{\rm high}$ (v3 has $R_{\rm high} = 1$ instead of 80), and included more spins (v3 only modeled 5 spin values $a_* \in \{-0.94, -0.5, 0, 0.5, 0.94\}$, compared with 13 spin values modeled in v5). In addition, v3 utilized an older `iharm` code (B. Prather et al. 2021) to evolve the fluid, compared with the newer KHARMA code used in v5.

The effect of each of these differences has yet to be fully assessed. However, the statistical characteristics of synthetic images can vary significantly between v3 and v5. The adiabatic index of $\gamma = 5/3$ in v5 produces higher temperatures in the emitting region than the lower adiabatic index of $\gamma = 4/3$ in v3. The higher adiabatic index of the v5 library analyzed in the body of this text is considered more accurate (C. F. Gammie 2025).

In Figure 9, we show the asymmetry dependence for v3 and v5 models, again marginalizing across the radiative transfer parameters $R_{\rm high}$ and $R_{\rm low}$ as above. Despite differences, the v3 model library generally produces similar trends to v5. Both are maximized at $|a_*| \approx 1$ and minimized at $|a_*| \ll 1$. One interesting feature of the v3 models is that the minimum in median asymmetry occurs at $a_* = -0.5$, which is different from the minimum at $a_* = 0$ in v5. The reason for this difference is likely due to different velocity profiles in the emission region. The outdated, lower adiabatic index is expected to enable faster rotation (See the Appendix of N. S. Conroy et al. 2025). Then for v3 $a_* = -0.5$, Doppler beaming may contribute brighter emission on the side of approaching disk and receding spin, counteracting the effects of the moderate retrograde spin to create a more symmetric ring. However, we note the v3 library has no spins sampled between $a_* = 0$ and -0.5, so it is possible a denser sampling of spins would produce a closer minimum.

A.2. SANE Models

We also show the brightness asymmetry in SANEs in Figure 9. In both model libraries, the mean asymmetry is larger for prograde SANEs than retrograde SANEs, in contrast to MADs where the distribution is more symmetrical. In SANEs, the rotation curve is nearly Keplerian, while MADs have strongly sub-Keplerian rotation curves (N. S. Conroy et al. 2023; V. Dhruv et al. 2025). Thus, Doppler beaming plays a larger role in SANEs relative to lensing, increasing the asymmetry for prograde models.[173] This makes SANEs better agree with observed asymmetries of M87* at more modest positive spin values. For retrograde models, Doppler beaming and lensing compete (along with other effects) to produce asymmetry in opposite hemispheres.

Appendix B
m-ring Truncation, Asymmetry Bounds, and (u, v) Coverage

For the bulk of this analysis, we used an *m*-ring model that was truncated at $m = 4$, bound by asymmetry $a_m \in [0, 1)$, and fit in the (u, v) domain assuming 2018 (u, v) coverage. In this section, we show that changes to these specific methodology choices do not affect our spin constraints.

Our $m = 4$ *m*-ring had zero ellipticity and was allowed a single nuisance Gaussian, which models diffuse off-ring emission. Geometric ring models are well-motivated for EHT sources (e.g., EHTC M87 IV; P. Tiede 2022; P. Tiede et al. 2022), especially *m*-rings with $m \in \{2, 3, 4\}$. The addition of a nuisance Gaussian improves the fit of the model (EHTC M87 2018 I, Figure 14). Here, for simplicity, we considered a single Comrade template. Would different choices of geometric model template, parameter bounds, or simulated (u, v) coverage change our results?

Figure 10 shows a two-sample KS test as done in Figure 6, this time while varying assumed (u, v) coverage from 2017 to 2021, the assumed parameter bounds from $a_{1\,\rm max} = 1$ to 1.5, and the geometric model template from an $m = 4$ *m*-ring to an $m = 3$ one. This analysis was performed at a reduced cadence of one frame every $500\,t_g$, leaving 60 samples for each unique model, and 480 for each unique spin. The changes in asymmetry bounds or assumed (u, v) coverage have a negligible effect on *p*-values.

A small subset of MAD model frames (2.6% of all MAD frames, 0.3% of MAD $|a_*| \leqslant 0.5$ frames) have asymmetry near the boundary ($a_1 > 0.99$, as is visible in Figure 3). These are most common in high-spin models with a large brightness peak. By visual inspection of GRMHD frames, $a_1 \simeq 1$ occurs when the dim side of the ring is particularly dim, or when the ring appears obscured with a large amount of extended emission. In this case, setting a higher asymmetry bound allows us to capture the tail of asymmetry distribution in $|a_*| \sim 1$ models. Although $a_1 > 1$ would appear to permit negative intensity on the faint side of the ring, the optimizer prevents this by aligning the phase of higher-order *m*-rings and the nuisance Gaussian. Thus, recovering such large asymmetry

[173] Note that asymmetry measurements for v5 SANEs at $a_* = 0.85$ and 0.97 were calculated over a shorter duration ($t = 20{,}000$ to $30{,}000\,t_g$ rather than 20,000 to $50{,}000\,t_g$), with a slightly higher cadence (every $100\,t_g$ rather than every $125\,t_g$), using a reduced image resolution. These differences may account for the wider 1σ region for those models.

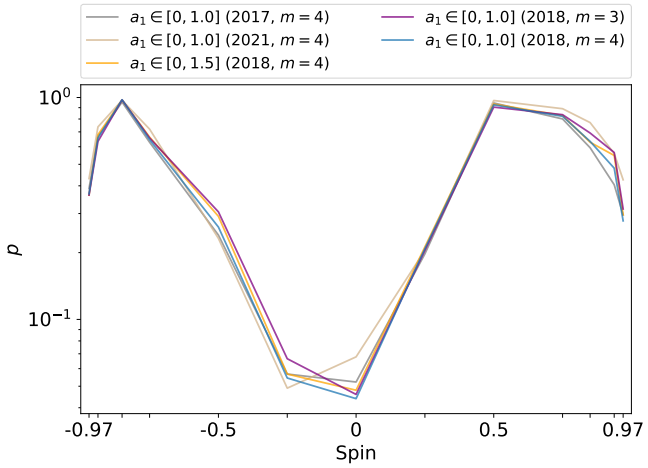

Figure 10. Same as Figure 6, but now showing the probability p across spin for the two-sample KS test using different modeling methodologies. We replot the curve of Figure 6 (blue), adjust the assumed (u, v) coverage from 2018 to 2017 (gray) and 2021 (tan), adjust the Comrade template to allow a maximum asymmetry of $a_{1\,\max} = 1.5$ (orange), and adjust the Comrade template to use an $m = 3$ m-ring (purple). The results are largely consistent, producing lower p-values for zero-spin models.

requires accurate recovery of the higher-order m-ring harmonics.

Rather than shifting the bound of the truncated Gaussian, one might also consider fitting a clipped Gaussian distribution, where the values outside of $a_1 = 1$ are reflected across the threshold. We tried fitting a clipped Gaussian and found this had little effect on the recovered μ for each model. In any event, current measurements of asymmetry observations are far from the $a_1 = 1$ boundary, and raising the boundary has negligible effect on p-values.

Finally, we tried fitting an $m = 3$ ring to observations and compared with the distribution found in models at each spin and again found largely consistent results. Zero-spin models produce a low p-value. We conclude that our spin constraints are relatively insensitive to details of the geometric model. As suggested by Figure 8, if the true spin magnitude of M87* is far enough from zero, we will be able to more confidently rule out zero-spin models using future observations.

Appendix C
Asymmetry Fits from GRMHD Library

Table 3 provides the mode μ and the standard deviation σ of the truncated Gaussian fits to each model in the v5 M87* library. The model parameters are summarized in Table 1. As in Table 2, we filter out the small percentage of frames that have an asymmetry equal to the bound when fitting the truncated normal parameters. A small fraction of high-spin SANEs are poorly fit, as the asymmetry boundary truncates a significant portion of the asymmetry distribution. Nevertheless, the chosen bounds generally improve fitting accuracy, and have negligible effects on observational constraints. See Appendices A and B for discussion.

Table 3
Gaussian Fits to Asymmetry for All Models

MAD/SANE	a_*	i (deg)	$R_{\rm high}$	$R_{\rm low}$	μ	σ
MAD	−0.97	17	10	1	0.612	0.192
MAD	−0.97	17	10	10	0.622	0.214
MAD	−0.97	17	40	1	0.671	0.194
MAD	−0.97	17	40	10	0.663	0.214
MAD	−0.97	17	80	1	0.671	0.189
MAD	−0.97	17	80	10	0.656	0.201
MAD	−0.97	17	160	1	0.674	0.207
MAD	−0.97	17	160	10	0.661	0.207

Note. Truncated Gaussian fits to asymmetry distributions of individual GRMHD models in v5 library. Each model is specified by its magnetic field mode (MAD/SANE), spin a_*, observer inclination i, and electron temperature parameters $R_{\rm high}$ and $R_{\rm low}$. The fitted mode μ and standard deviation σ are shown. Only a portion of this table is shown here to demonstrate its form and content.

(This table is available in its entirety in machine-readable form in the online article.)

ORCID iDs

Vadim Bernshteyn https://orcid.org/0009-0000-1376-2352
Nicholas S. Conroy https://orcid.org/0000-0003-2886-2377
Michi Bauböck https://orcid.org/0000-0002-5518-2812
Paul Tiede https://orcid.org/0000-0003-3826-5648
Abhishek V. Joshi https://orcid.org/0000-0002-2514-5965
Ben S. Prather https://orcid.org/0000-0002-0393-7734
Charles F. Gammie https://orcid.org/0000-0001-7451-8935
Kazunori Akiyama https://orcid.org/0000-0002-9475-4254
Ezequiel Albentosa-Ruíz https://orcid.org/0000-0002-7816-6401
Antxon Alberdi https://orcid.org/0000-0002-9371-1033
Juan Carlos Algaba https://orcid.org/0000-0001-6993-1696
Richard Anantua https://orcid.org/0000-0003-3457-7660
Keiichi Asada https://orcid.org/0000-0001-6988-8763
Rebecca Azulay https://orcid.org/0000-0002-2200-5393
Anne-Kathrin Baczko https://orcid.org/0000-0003-3090-3975

Bidisha Bandyopadhyay https://orcid.org/0000-0002-2138-8564
John Barrett https://orcid.org/0000-0002-9290-0764
Bradford A. Benson https://orcid.org/0000-0002-5108-6823
Lindy Blackburn https://orcid.org/0000-0002-9030-642X
Raymond Blundell https://orcid.org/0000-0002-5929-5857
Katherine L. Bouman https://orcid.org/0000-0003-0077-4367
Geoffrey C. Bower https://orcid.org/0000-0003-4056-9982
Michael Bremer https://orcid.org/0000-0001-7511-3745
Roger Brissenden https://orcid.org/0000-0002-2556-0894
Silke Britzen https://orcid.org/0000-0001-9240-6734
Avery E. Broderick https://orcid.org/0000-0002-3351-760X
Dominique Broguiere https://orcid.org/0000-0001-9151-6683
Thomas Bronzwaer https://orcid.org/0000-0003-1151-3971
Sandra Bustamante https://orcid.org/0000-0001-6169-1894
Douglas F. Carlos https://orcid.org/0000-0002-1340-7702
John E. Carlstrom https://orcid.org/0000-0002-2044-7665
Andrew Chael https://orcid.org/0000-0003-2966-6220
Chi-kwan Chan https://orcid.org/0000-0001-6337-6126
Dominic O. Chang https://orcid.org/0000-0001-9939-5257
Koushik Chatterjee https://orcid.org/0000-0002-2825-3590
Ming-Tang Chen https://orcid.org/0000-0001-6573-3318
Yongjun Chen (陈永军) https://orcid.org/0000-0001-5650-6770
Xiaopeng Cheng https://orcid.org/0000-0003-4407-9868
Paul Chichura https://orcid.org/0000-0002-5397-9035
Ilje Cho https://orcid.org/0000-0001-6083-7521
John E. Conway https://orcid.org/0000-0003-2448-9181
Thomas M. Crawford https://orcid.org/0000-0001-9000-5013
Geoffrey B. Crew https://orcid.org/0000-0002-2079-3189
Alejandro Cruz-Osorio https://orcid.org/0000-0002-3945-6342
Yuzhu Cui (崔玉竹) https://orcid.org/0000-0001-6311-4345
Brandon Curd https://orcid.org/0000-0002-8650-0879
Rohan Dahale https://orcid.org/0000-0001-6982-9034
Jordy Davelaar https://orcid.org/0000-0002-2685-2434
Mariafelicia De Laurentis https://orcid.org/0000-0002-9945-682X
Roger Deane https://orcid.org/0000-0003-1027-5043
Jason Dexter https://orcid.org/0000-0003-3903-0373
Vedant Dhruv https://orcid.org/0000-0001-6765-877X
Indu K. Dihingia https://orcid.org/0000-0002-4064-0446
Sheperd S. Doeleman https://orcid.org/0000-0002-9031-0904
Sergio A. Dzib https://orcid.org/0000-0001-6010-6200
Razieh Emami https://orcid.org/0000-0002-2791-5011
Heino Falcke https://orcid.org/0000-0002-2526-6724
Joseph Farah https://orcid.org/0000-0003-4914-5625
Vincent L. Fish https://orcid.org/0000-0002-7128-9345
Edward Fomalont https://orcid.org/0000-0002-9036-2747
H. Alyson Ford https://orcid.org/0000-0002-9797-0972
Marianna Foschi https://orcid.org/0000-0001-8147-4993
Raquel Fraga-Encinas https://orcid.org/0000-0002-5222-1361
Per Friberg https://orcid.org/0000-0002-8010-8454
Christian M. Fromm https://orcid.org/0000-0002-1827-1656
Antonio Fuentes https://orcid.org/0000-0002-8773-4933
Peter Galison https://orcid.org/0000-0002-6429-3872
Roberto García https://orcid.org/0000-0002-6584-7443
Olivier Gentaz https://orcid.org/0000-0002-0115-4605
Boris Georgiev https://orcid.org/0000-0002-3586-6424
Ciriaco Goddi https://orcid.org/0000-0002-2542-7743
Roman Gold https://orcid.org/0000-0003-2492-1966
Arturo I. Gómez-Ruiz https://orcid.org/0000-0001-9395-1670
José L. Gómez https://orcid.org/0000-0003-4190-7613
Minfeng Gu (顾敏峰) https://orcid.org/0000-0002-4455-6946
Mark Gurwell https://orcid.org/0000-0003-0685-3621
Kazuhiro Hada https://orcid.org/0000-0001-6906-772X
Daryl Haggard https://orcid.org/0000-0001-6803-2138
Ronald Hesper https://orcid.org/0000-0003-1918-6098
Dirk Heumann https://orcid.org/0000-0002-7671-0047
Luis C. Ho (何子山) https://orcid.org/0000-0001-6947-5846
Paul Ho https://orcid.org/0000-0002-3412-4306
Mareki Honma https://orcid.org/0000-0003-4058-9000
Chih-Wei L. Huang https://orcid.org/0000-0001-5641-3953
Lei Huang (黄磊) https://orcid.org/0000-0002-1923-227X
Shiro Ikeda https://orcid.org/0000-0002-2462-1448
C. M. Violette Impellizzeri https://orcid.org/0000-0002-3443-2472
Makoto Inoue https://orcid.org/0000-0001-5037-3989
Sara Issaoun https://orcid.org/0000-0002-5297-921X
David J. James https://orcid.org/0000-0001-5160-4486
Buell T. Jannuzi https://orcid.org/0000-0002-1578-6582
Michael Janssen https://orcid.org/0000-0001-8685-6544
Britton Jeter https://orcid.org/0000-0003-2847-1712
Wu Jiang (江悟) https://orcid.org/0000-0001-7369-3539
Alejandra Jiménez-Rosales https://orcid.org/0000-0002-2662-3754
Michael D. Johnson https://orcid.org/0000-0002-4120-3029
Svetlana Jorstad https://orcid.org/0000-0001-6158-1708
Taehyun Jung https://orcid.org/0000-0001-7003-8643
Tomohisa Kawashima https://orcid.org/0000-0001-8527-0496
Garrett K. Keating https://orcid.org/0000-0002-3490-146X
Mark Kettenis https://orcid.org/0000-0002-6156-5617
Dong-Jin Kim https://orcid.org/0000-0002-7038-2118
Jae-Young Kim https://orcid.org/0000-0001-8229-7183
Jongsoo Kim https://orcid.org/0000-0002-1229-0426
Junhan Kim https://orcid.org/0000-0002-4274-9373
Motoki Kino https://orcid.org/0000-0002-2709-7338
Jun Yi Koay https://orcid.org/0000-0002-7029-6658
Prashant Kocherlakota https://orcid.org/0000-0001-7386-7439
Patrick M. Koch https://orcid.org/0000-0003-2777-5861
Shoko Koyama https://orcid.org/0000-0002-3723-3372
Carsten Kramer https://orcid.org/0000-0002-4908-4925
Joana A. Kramer https://orcid.org/0009-0003-3011-0454
Michael Kramer https://orcid.org/0000-0002-4175-2271
Thomas P. Krichbaum https://orcid.org/0000-0002-4892-9586
Cheng-Yu Kuo https://orcid.org/0000-0001-6211-5581
Noemi La Bella https://orcid.org/0000-0002-8116-9427
Deokhyeong Lee https://orcid.org/0009-0003-2122-9437
Sang-Sung Lee https://orcid.org/0000-0002-6269-594X
Aviad Levis https://orcid.org/0000-0001-7307-632X
Shaoliang Li https://orcid.org/0009-0005-0338-9490
Zhiyuan Li (李志远) https://orcid.org/0000-0003-0355-6437

Rocco Lico https://orcid.org/0000-0001-7361-2460
Greg Lindahl https://orcid.org/0000-0002-6100-4772
Michael Lindqvist https://orcid.org/0000-0002-3669-0715
Mikhail Lisakov https://orcid.org/0000-0001-6088-3819
Jun Liu (刘俊) https://orcid.org/0000-0002-7615-7499
Kuo Liu https://orcid.org/0000-0002-2953-7376
Elisabetta Liuzzo https://orcid.org/0000-0003-0995-5201
Wen-Ping Lo https://orcid.org/0000-0003-1869-2503
Andrei P. Lobanov https://orcid.org/0000-0003-1622-1484
Laurent Loinard https://orcid.org/0000-0002-5635-3345
Colin J. Lonsdale https://orcid.org/0000-0003-4062-4654
Amy E. Lowitz https://orcid.org/0000-0002-4747-4276
Ru-Sen Lu (路如森) https://orcid.org/0000-0002-7692-7967
Nicholas R. MacDonald https://orcid.org/0000-0002-6684-8691
Jirong Mao (毛基荣) https://orcid.org/0000-0002-7077-7195
Nicola Marchili https://orcid.org/0000-0002-5523-7588
Sera Markoff https://orcid.org/0000-0001-9564-0876
Daniel P. Marrone https://orcid.org/0000-0002-2367-1080
Alan P. Marscher https://orcid.org/0000-0001-7396-3332
Iván Martí-Vidal https://orcid.org/0000-0003-3708-9611
Satoki Matsushita https://orcid.org/0000-0002-2127-7880
Lynn D. Matthews https://orcid.org/0000-0002-3728-8082
Lia Medeiros https://orcid.org/0000-0003-2342-6728
Karl M. Menten https://orcid.org/0000-0001-6459-0669
Hugo Messias https://orcid.org/0000-0002-2985-7994
Izumi Mizuno https://orcid.org/0000-0002-7210-6264
Yosuke Mizuno https://orcid.org/0000-0002-8131-6730
Joshua Montgomery https://orcid.org/0000-0003-0345-8386
Kotaro Moriyama https://orcid.org/0000-0003-1364-3761
Monika Moscibrodzka https://orcid.org/0000-0002-4661-6332
Wanga Mulaudzi https://orcid.org/0000-0003-4514-625X
Cornelia Müller https://orcid.org/0000-0002-2739-2994
Hendrik Müller https://orcid.org/0000-0002-9250-0197
Alejandro Mus https://orcid.org/0000-0003-0329-6874
Gibwa Musoke https://orcid.org/0000-0003-1984-189X
Ioannis Myserlis https://orcid.org/0000-0003-3025-9497
Hiroshi Nagai https://orcid.org/0000-0003-0292-3645
Neil M. Nagar https://orcid.org/0000-0001-6920-662X
Dhanya G. Nair https://orcid.org/0000-0001-5357-7805
Masanori Nakamura https://orcid.org/0000-0001-6081-2420
Gopal Narayanan https://orcid.org/0000-0002-4723-6569
Iniyan Natarajan https://orcid.org/0000-0001-8242-4373
Antonios Nathanail https://orcid.org/0000-0002-1655-9912
Joey Neilsen https://orcid.org/0000-0002-8247-786X
Chunchong Ni https://orcid.org/0000-0003-1361-5699
Michael A. Nowak https://orcid.org/0000-0001-6923-1315
Hiroki Okino https://orcid.org/0000-0003-3779-2016
Héctor Raúl Olivares Sánchez https://orcid.org/0000-0001-6833-7580
Feryal Özel https://orcid.org/0000-0003-4413-1523
Daniel C. M. Palumbo https://orcid.org/0000-0002-7179-3816
Georgios Filippos Paraschos https://orcid.org/0000-0001-6757-3098
Jongho Park https://orcid.org/0000-0001-6558-9053
Harriet Parsons https://orcid.org/0000-0002-6327-3423
Nimesh Patel https://orcid.org/0000-0002-6021-9421
Ue-Li Pen https://orcid.org/0000-0003-2155-9578
Dominic W. Pesce https://orcid.org/0000-0002-5278-9221
Vincent Piétu https://orcid.org/0009-0006-3497-397X
Alexander Plavin https://orcid.org/0000-0003-2914-8554
Oliver Porth https://orcid.org/0000-0002-4584-2557
Giacomo Principe https://orcid.org/0000-0003-0406-7387
Dimitrios Psaltis https://orcid.org/0000-0003-1035-3240
Hung-Yi Pu https://orcid.org/0000-0001-9270-8812
Alexandra Rahlin https://orcid.org/0000-0003-3953-1776
Venkatessh Ramakrishnan https://orcid.org/0000-0002-9248-086X
Ramprasad Rao https://orcid.org/0000-0002-1407-7944
Mark G. Rawlings https://orcid.org/0000-0002-6529-202X
Luciano Rezzolla https://orcid.org/0000-0002-1330-7103
Angelo Ricarte https://orcid.org/0000-0001-5287-0452
Luca Ricci https://orcid.org/0000-0002-4175-3194
Bart Ripperda https://orcid.org/0000-0002-7301-3908
Jan Röder https://orcid.org/0000-0002-2426-927X
Freek Roelofs https://orcid.org/0000-0001-5461-3687
Cristina Romero-Cañizales https://orcid.org/0000-0001-6301-9073
Eduardo Ros https://orcid.org/0000-0001-9503-4892
Arash Roshanineshat https://orcid.org/0000-0002-8280-9238
Alan L. Roy https://orcid.org/0000-0002-1931-0135
Ignacio Ruiz https://orcid.org/0000-0002-0965-5463
Chet Ruszczyk https://orcid.org/0000-0001-7278-9707
Kazi L. J. Rygl https://orcid.org/0000-0003-4146-9043
León D. S. Salas https://orcid.org/0000-0003-1979-6363
Salvador Sánchez https://orcid.org/0000-0002-8042-5951
David Sánchez-Argüelles https://orcid.org/0000-0002-7344-9920
Miguel Sánchez-Portal https://orcid.org/0000-0003-0981-9664
Mahito Sasada https://orcid.org/0000-0001-5946-9960
Kaushik Satapathy https://orcid.org/0000-0003-0433-3585
Saurabh https://orcid.org/0000-0001-7156-4848
Tuomas Savolainen https://orcid.org/0000-0001-6214-1085
Karl-Friedrich Schuster https://orcid.org/0000-0003-2890-9454
Zhiqiang Shen (沈志强) https://orcid.org/0000-0003-3540-8746
Sasikumar Silpa https://orcid.org/0000-0003-0667-7074
Randall Smith https://orcid.org/0000-0003-4284-4167
Bong Won Sohn https://orcid.org/0000-0002-4148-8378
Jason SooHoo https://orcid.org/0000-0003-1938-0720
Kamal Souccar https://orcid.org/0000-0001-7915-5272
Joshua S. Stanway https://orcid.org/0009-0003-7659-4642
He Sun (孙赫) https://orcid.org/0000-0003-1526-6787
Alexandra J. Tetarenko https://orcid.org/0000-0003-3906-4354
Remo P. J. Tilanus https://orcid.org/0000-0002-6514-553X
Michael Titus https://orcid.org/0000-0001-9001-3275
Kenji Toma https://orcid.org/0000-0002-7114-6010
Pablo Torne https://orcid.org/0000-0001-8700-6058
Teresa Toscano https://orcid.org/0000-0003-3658-7862
Efthalia Traianou https://orcid.org/0000-0002-1209-6500
Sascha Trippe https://orcid.org/0000-0003-0465-1559
Matthew Turk https://orcid.org/0000-0002-5294-0198
Ilse van Bemmel https://orcid.org/0000-0001-5473-2950
Huib Jan van Langevelde https://orcid.org/0000-0002-0230-5946
Daniel R. van Rossum https://orcid.org/0000-0001-7772-6131
Sebastiano D. von Fellenberg https://orcid.org/0000-0002-9156-2249
Jesse Vos https://orcid.org/0000-0003-3349-7394
Jan Wagner https://orcid.org/0000-0003-1105-6109
Derek Ward-Thompson https://orcid.org/0000-0003-1140-2761

John Wardle https://orcid.org/0000-0002-8960-2942
Jasmin E. Washington https://orcid.org/0000-0002-7046-0470
Jonathan Weintroub https://orcid.org/0000-0002-4603-5204
Maciek Wielgus https://orcid.org/0000-0002-8635-4242
Kaj Wiik https://orcid.org/0000-0002-0862-3398
Michael F. Wondrak https://orcid.org/0000-0002-6894-1072
George N. Wong https://orcid.org/0000-0001-6952-2147
Jompoj Wongphexhauxsorn https://orcid.org/0000-0002-7730-4956
Qingwen Wu (吴庆文) https://orcid.org/0000-0003-4773-4987
Paul Yamaguchi https://orcid.org/0000-0002-6017-8199
Aristomenis Yfantis https://orcid.org/0000-0002-3244-7072
Doosoo Yoon https://orcid.org/0000-0001-8694-8166
André Young https://orcid.org/0000-0003-0000-2682
Ziri Younsi https://orcid.org/0000-0001-9283-1191
Wei Yu (于威) https://orcid.org/0000-0002-5168-6052
Feng Yuan (袁峰) https://orcid.org/0000-0003-3564-6437
Ye-Fei Yuan (袁业飞) https://orcid.org/0000-0002-7330-4756
Ai-Ling Zeng (曾艾玲) https://orcid.org/0009-0000-9427-4608
J. Anton Zensus https://orcid.org/0000-0001-7470-3321
Shuo Zhang https://orcid.org/0000-0002-2967-790X
Guang-Yao Zhao https://orcid.org/0000-0002-4417-1659

References

Bambi, C., Brenneman, L. W., Dauser, T., et al. 2021, SSRv, 217, 65
Bardeen, J. M., & Petterson, J. A. 1975, ApJL, 195, L65
Blandford, R. D., & Payne, D. G. 1982, MNRAS, 199, 883
Blandford, R. D., & Znajek, R. L. 1977, MNRAS, 179, 433
Chael, A. 2025, MNRAS, 537, 2496
Chael, A., Lupsasca, A., Wong, G. N., & Quataert, E. 2023, ApJ, 958, 65
Chael, A. A., Johnson, M. D., Bouman, K. L., et al. 2018, ApJ, 857, 23
Conroy, N. S., Bauböck, M., Dhruv, V., et al. 2023, ApJ, 951, 46
Conroy, N. S., Bauböck, M., Dhruv, V., et al. 2025, arXiv:2510.08848
Dhruv, V., Prather, B., Chandra, M., Joshi, A. V., & Gammie, C. F. 2025, ApJL, 993, L33
Dhruv, V., Prather, B., Wong, G., & Gammie, C. F. 2025, ApJS, 277, 16
Di Matteo, T., Allen, S. W., Fabian, A. C., Wilson, A. S., & Young, A. J. 2003, ApJ, 582, 133
Event Horizon Telescope Collaboration, Akiyama, K., Albentosa-Ruíz, E., et al. 2025a, A&A, 693, A265
Event Horizon Telescope Collaboration, Akiyama, K., Albentosa-Ruíz, E., et al. 2025b, A&A, 704, 91
Event Horizon Telescope Collaboration, Akiyama, K., Alberdi, A., et al. 2019a, ApJL, 875, L1
Event Horizon Telescope Collaboration, Akiyama, K., Alberdi, A., et al. 2019b, ApJL, 875, L2
Event Horizon Telescope Collaboration, Akiyama, K., Alberdi, A., et al. 2019c, ApJL, 875, L3
Event Horizon Telescope Collaboration, Akiyama, K., Alberdi, A., et al. 2019d, ApJL, 875, L4
Event Horizon Telescope Collaboration, Akiyama, K., Alberdi, A., et al. 2019e, ApJL, 875, L5
Event Horizon Telescope Collaboration, Akiyama, K., Alberdi, A., et al. 2019f, ApJL, 875, L6
Event Horizon Telescope Collaboration, Akiyama, K., Alberdi, A., et al. 2022, ApJ, 930, L16
Event Horizon Telescope Collaboration, Akiyama, K., Alberdi, A., et al. 2023, ApJ, 957, L20
Event Horizon Telescope Collaboration, Akiyama, K., Alberdi, A., et al. 2024, A&A, 681, A79
Event Horizon Telescope Collaboration, Akiyama, K., Algaba, J. C., et al. 2021, ApJL, 910, L13
Faggert, J. C., Özel, F., & Psaltis, D. 2025, ApJ, 981, 209
Fishbone, L. G., & Moncrief, V. 1976, ApJ, 207, 962
Foucart, F., Chandra, M., Gammie, C. F., Quataert, E., & Tchekhovskoy, A. 2017, MNRAS, 470, 2240
Fragile, P. C., & Anninos, P. 2005, ApJ, 623, 347
Fragile, P. C., Blaes, O. M., Anninos, P., & Salmonson, J. D. 2007, ApJ, 668, 417
Galishnikova, A., Philippov, A., & Quataert, E. 2023, ApJ, 957, 103
Gammie, C. F. 2025, ApJ, 980, 193
Gammie, C. F., Shapiro, S. L., & McKinney, J. C. 2004, ApJ, 602, 312
Gebhardt, K., Adams, J., Richstone, D., et al. 2011, ApJ, 729, 119
Ginzburg, V. L., & Syrovatskii, S. I. 1965, ARA&A, 3, 297
Grete, P., O'Shea, B. W., & Beckwith, K. 2023, ApJL, 942, L34
Ichimaru, S. 1977, ApJ, 214, 840
Igumenshchev, I. V., Narayan, R., & Abramowicz, M. A. 2003, ApJ, 592, 1042
Janssen, M., Chan, C. K., Davelaar, J., & Wielgus, M. 2025, A&A, 698, A62
Johnson, M. D., Akiyama, K., Baturin, R., et al. 2024, Proc. SPIE, 13092, 130922
Johnson, M. D., Lupsasca, A., Strominger, A., et al. 2020, SciA, 6, eaaz1310
Kerr, R. P. 1963, PhRvL, 11, 237
Kunz, M. W., Schekochihin, A. A., & Stone, J. M. 2014, PhRvL, 112, 205003
Levin, Y. 2024, ApJ, 975, 278
Levin, Y., & Beloborodov, A. M. 2003, ApJL, 590, L33
Liepold, E. R., Ma, C.-P., & Walsh, J. L. 2023, ApJL, 945, L35
Liska, M., Hesp, C., Tchekhovskoy, A., et al. 2018, MNRAS, 474, L81
Lu, R.-S., Asada, K., Krichbaum, T. P., et al. 2023, Natur, 616, 686
Lynden-Bell, D., & Boily, C. 1994, MNRAS, 267, 146
McKinney, J. C., & Gammie, C. F. 2004, ApJ, 611, 977
Medeiros, L., Chan, C.-K., Narayan, R., Özel, F., & Psaltis, D. 2022, ApJ, 924, 46
Merloni, A., & Heinz, S. 2008, MNRAS, 388, 1011
Mertens, F., Lobanov, A. P., Walker, R. C., & Hardee, P. E. 2016, A&A, 595, A54
Mościbrodzka, M., Falcke, H., & Shiokawa, H. 2016, A&A, 586, A38
Mościbrodzka, M., & Gammie, C. F. 2018, MNRAS, 475, 43
Narayan, R., Igumenshchev, I. V., & Abramowicz, M. A. 2003, PASJ, 55, L69
Narayan, R., SÄ dowski, A., Penna, R. F., & Kulkarni, A. K. 2012, MNRAS, 426, 3241
Narayan, R., & Yi, I. 1994, ApJL, 428, L13
Narayan, R., & Yi, I. 1995, ApJ, 452, 710
Narayan, R., Yi, I., & Mahadevan, R. 1995, Natur, 374, 623
Nemmen, R. 2019, ApJL, 880, L26
Pacucci, F., & Loeb, A. 2020, ApJ, 895, 95
Palumbo, D. C. M., Wong, G. N., & Prather, B. S. 2020, ApJ, 894, 156
Pordes, R., , OSG Consortium, Petravick, D., et al. 2007, JPhCS, 78, 012057
Prather, B., Wong, G., Dhruv, V., et al. 2021, JOSS, 6, 3336
Prather, B. S. 2025, in New Frontiers in GRMHD Simulations, ed. C. Bambi, Y. Mizuno, S. Shashank, & F. Yuan (Springer), 167
Qiu, R., Ricarte, A., Narayan, R., et al. 2023, MNRAS, 520, 4867
Quataert, E., & Narayan, R. 1999, ApJ, 520, 298
Rees, M. J., Begelman, M. C., & Blandford, R. D. 1981, NYASA, 375, 254
Rees, M. J., Begelman, M. C., Blandford, R. D., & Phinney, E. S. 1982, Natur, 295, 17
Ressler, S. M., White, C. J., Quataert, E., & Stone, J. M. 2020, ApJL, 896, L6
Reynolds, C. S. 2021, ARA&A, 59, 117
Reynolds, C. S., Di Matteo, T., Fabian, A. C., Hwang, U., & Canizares, C. R. 1996, MNRAS, 283, L111
Ricarte, A., Natarajan, P., Narayan, R., & Palumbo, D. C. M. 2025, ApJ, 980, 136
Ricarte, A., Tiede, P., Emami, R., Tamar, A., & Natarajan, P. 2023, Galax, 11, 6
Ripperda, B., Bacchini, F., & Philippov, A. A. 2020, ApJ, 900, 100
Roy, A. & OSG Consortium 2009, JPhCS, 180, 012052
Sądowski, A., Narayan, R., Penna, R., & Zhu, Y. 2013, MNRAS, 436, 3856
Sala, L., Valentini, M., Biffi, V., & Dolag, K. 2024, A&A, 685, A92
Salas, L., Liska, M., Markoff, S., et al. 2025, MNRAS, 538, 698
Saurabh, Wielgus, M, Tursunov, A., Lobanov, A. P., & Emami, R. 2026, A&A, 705, A166
Shiokawa, H. 2013, PhD thesis, Univ. Illinois, Urbana-Champaign
Tchekhovskoy, A., Narayan, R., & McKinney, J. C. 2011, MNRAS, 418, L79
Tiede, P. 2022, JOSS, 7, 4457
Tiede, P., Broderick, A. E., & Palumbo, D. C. M. 2022, ApJ, 925, 122
Walker, R. C., Hardee, P. E., Davies, F. B., Ly, C., & Junor, W. 2018, ApJ, 855, 128
Wong, G. N., Prather, B. S., Dhruv, V., et al. 2022, ApJS, 259, 64
Yuan, F., Markoff, S., Falcke, H., & Biermann, P. L. 2002, A&A, 391, 139
Yuan, F., & Narayan, R. 2014, ARA&A, 52, 529
Yuan, F., Quataert, E., & Narayan, R. 2003, ApJ, 598, 301
Zhang, X. A., Ricarte, A., Pesce, D. W., et al. 2024, ApJ, 985, 41